

Charles University in Prague
Faculty of Mathematics and Physics

DIPLOMA THESIS



Juraj Šibík

Application of metamaterial structures in terahertz spectral range

Department of Chemical Physics and Optics

Supervisor: RNDr. Petr Kužel, PhD.

Study program: Physics, Optics and Optoelectronics

2010

Rád by som poďakoval vedúcemu diplomovej práce Petrovi Kuželovi za výborné vedenie a nepretržitú ochotu pomôcť. Vďaka jeho podpore bola práca do veľkej miery aj zábavou. Ďakujem mu tiež za kritické čítanie diplomovej práce a množstvo návrhov na zlepšenie, čo posunulo prácu na vyššiu úroveň.

Veľká vďaka patrí Christelle Kadlec najmä za experimentálnu pomoc a morálnu podporu, ale tiež aj za dôležité diskusie pri návrhu štruktúr a vyhodnocovaní výsledkov. Experimentálna časť by nemohla byť uskutočnená bez Karine Blary z Univesity of Lille, ktorá vyrobila všetky navrhnuté vzorky a prispela tak neoceniteľnou časťou k práci. Ďakujem Hynkovi Němcovi za spočítanie nárastu indexu lomu v leptaných štruktúrach pomocou 3-D formalizmu prenosových matíc. Rád by som vyjadril poďakovanie všetkým členom Laboratoře Terahertzové Spektroskopie na FZÚ AV ČR v Prahe za ich podporu.

V neposlednom rade ďakujem rodine a všetkým priateľom za morálnu podporu a pomoc počas vykonávania práce.

Prohlašuji, že jsem svou diplomovou práci napsal samostatně a výhradně s použitím citovaných pramenů. Souhlasím se zapůjčováním práce a jejím zveřejňováním.

V Praze dne 27. dubna 2010

Juraj Šibík

Contents

Abstracts	v
1 Terahertz radiation and spectroscopy	1
1.1 Introduction	1
1.2 THz sources	2
1.3 THz detectors	4
1.4 Time domain THz spectroscopy	5
1.5 Industrial applications	6
2 Metamaterials	9
2.1 Principles and historical overview	9
2.2 Metamaterial structures and effective response	12
2.2.1 Quasi-static regime	13
2.2.2 Metamaterial resonances	15
2.3 Applications	18
3 Polarization of light	21
3.1 Polarization of light	21
3.2 Jones-vector representation	24
3.3 Wave retarders	25
3.3.1 Half-wave plate	25
3.3.2 Quarter-wave plate	26
4 Wave plates	27
4.1 Etched layers for THz radiation	27
4.2 Design of a wave plate	29
4.2.1 Layer C	29
4.2.2 Layers A and E	30
4.2.3 Layers B and D	31
4.3 Optimization of transmission	32
4.3.1 Transfer matrix formalism	32
4.3.2 Optimization results	33

5	Experiments and results	37
5.1	Experimental setup	37
5.2	Data processing	38
5.3	Anisotropy of an etched layer	42
5.4	Samples	46
5.4.1	Walls 20 microns	46
5.4.2	Walls 48 microns	47
5.4.3	Walls 119 microns	47
5.4.4	Pillars 40.5 microns	48
5.4.5	Pillars 81 microns	48
5.4.6	Summary	48
5.4.7	SEM photos and graphs	49
5.5	Antireflective bilayers	60
5.6	Wave plates	63
5.6.1	Quarter-wave plate for 0.5 THz	65
5.6.2	Quarter-wave plate for 1 THz	65
5.6.3	Half-wave plate for 1 THz	66
5.6.4	Double quarter-wave plate for 1 THz	66
5.6.5	Graphs	66
5.7	Next research	71
6	Conclusion	73
	Bibliography	75

Abstracts

Název práce: Použití metamateriálových struktur v terahertzové spektrální oblasti

Autor: Juraj Šibík

Katedra (ústav): Katedra Chemické Fyziky a Optiky

Vedoucí diplomové práce: RNDr. Petr Kužel, PhD.

e-mail vedoucího: kuzelp@fzu.cz

Abstrakt: Práce se věnuje výzkumu metamateriálů pro terahertzovou spektrální oblast vytvořených ze vzorků hluboko leptaného křemíku. Hlavním cílem je teoretické navrhnutí a experimentální realizace fázových destiček pro vybrané terahertzové frekvence. Destičky jsou vyrobeny z křemíkových substrátů s vyleptanou dvourozměrnou periodickou mikrostrukturou, jejíž elementární buňky jsou menší než vlnová délka použitého záření. Teoretický návrh je optimalizován pomocí formalismu přenosových matic. V práci jsou navrženy a charakterizovány čtvrtvlnné fázové destičky pro frekvence 0.5 a 1 THz a půlvlnná destička pro frekvenci 1 THz.

Klíčová slova: terahertzová spektrální oblast, metamateriál, fázová destička

Title: Application of metamaterial structures in terahertz spectral range

Author: Juraj Šibík

Department: Department of Chemical Physics and Optics

Supervisor: RNDr. Petr Kužel, PhD.

Supervisor's e-mail address: kuzelp@fzu.cz

Abstract: The thesis is devoted to a research on metamaterials for terahertz spectral range based on deeply etched silicon. The aim of the work is a theoretical conception and experimental realization of wave plates for selected terahertz frequencies. These wave plates are made of silicon substrates with an etched two-dimensional periodic microstructure where the dimensions of an elementary cell are below the considered wavelength. Theoretical proposal is optimized using the transfer matrix formalism. We designed and experimentally characterized quarter-wave plates for frequencies 0.5 THz and 1 THz and a half-wave plate for frequency 1 THz.

Keywords: terahertz spectral range, metamaterial, wave plate

Chapter 1

Terahertz radiation and spectroscopy

1.1 Introduction

Terahertz (THz) radiation fills the gap between the infrared and microwave radiation, i.e. spectral range between 10^{11} Hz and 10^{13} Hz. THz radiation is non-ionizing, non-destructive and low energy radiation. Given that 1 THz corresponds to black body radiation at 48 K, it means no threat to human body, because all living objects are hotter and therefore they are sources of THz radiation.

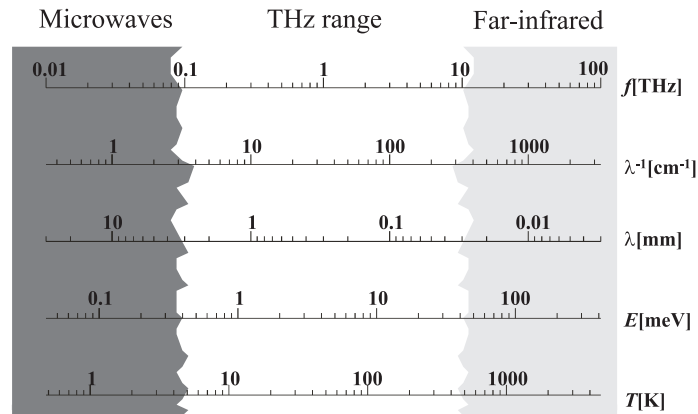


Figure 1.1: Spectrum of electromagnetic radiation. After Ref. [1]

However, eligible THz sources are available only for around 20 years. For the lower frequencies, including AM and FM radio frequencies up to microwave,

sources are based on classical electron transport. For higher frequencies, including infrared radiation, visible light and ultra violet radiation, sources are based on quantum transitions. For a long time THz range was not accessible neither from electrical nor optical part of the spectrum. The exploration boom of the THz started when a new method for the production and detection of bright coherent THz pulses using ultrafast optical pulses were introduced (so called opto-electronic approach to the THz spectroscopy).

1.2 THz sources

Photoconductive switches (photoconductive antennae) are one of the broadband THz sources and they were introduced for generation of THz pulses by Auston et al. [2]. A photoconductive antenna consists of two metal electrodes deposited on a semiconductor substrate. A short (~ 100 fs) optical pulse illuminates the gap between the electrodes and generates photocarriers. Subsequently the free carriers are accelerated in bias electric field. The rapid variation of the current density rises a THz pulse. The carriers are then trapped or recombined and the current density returns to its steady-state value. The lifetime of the free carriers is crucial since the current density has to reach a steady-state value before the next excitation pulse occurs.

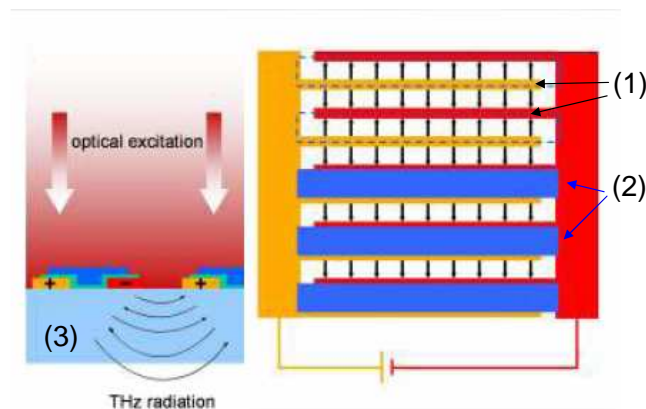


Figure 1.2: Photoswitch TeraSED. (1) Interdigitated electrode structure. (2) Optically opaque shielding of odd gaps between the electrode fingers. (3) GaAs substrate.

Later on, a photoswitch consisting of an integrated interdigital metal electrode structure was introduced [3], see Fig. 1.2. Every odd gap between the electrodes is shielded so the free carriers are not generated there. As a result carriers

are generated only in the parts of emitter with the same orientation of the bias electric field. The device can be decomposed into a lot of small emitters emitting THz radiation simultaneously and with the same phase.

Another way of generating broadband THz radiation is using a nonlinear medium for *optical rectification* [4] and *difference frequency generation*. Both these are second order nonlinear optical processes in which a THz photon of frequency ω_t is created by two optical photons ω_1, ω_2 such that $\omega_t = |\omega_1 - \omega_2|$. The mixing occurs between the frequencies within the ultrashort femtosecond pulse used as a source. Thus the shorter optical pulses are used, the broader THz spectrum will be generated.

One of the monochromatic types of THz sources are *quantum cascade lasers* (QCLs). QCL is a semiconductor heterostructure device composed of periodic series of semiconductor thin layers forming a superlattice (see Fig. 1.3). In typical interband semiconductor lasers the emission is based on the recombination of electron-hole pairs across the band gap, but the emission of QCL is achieved by intersubband transitions. By using a suitable thicknesses of the layers the active region and injector region can be engineered. The active region has discrete electronic level and injector region has electronic subbands, both are shifted by a voltage applied to the structure and electrons from injector region fill the upper lasing level of the active region thus creating a population inversion. The electrons then fall to the lower energy level of the active region emitting a low-energy photon. After that they are injected into the next active region and the procedure repeats. As a result one electron creates typically 25 to 75 photons per cascade transit. Photon emission in THz spectral range is achieved by appropriately positioned energy levels in the active region.

QCL can work in pulsed as well as in continuous regime. However, the QCL can work only at a low temperatures for now. The average output power of QCL dramatically decreases with increasing the temperature but at liquid helium temperature the output power reaches up to 100 mW. At present, the highest operation temperature of THz QCLs is around 180 K [5].

Technique	Mean power	Freq. range	Tunability	Pulse vs. CW
THz-TDS	5 μ W - 1 mW	0.1 - 5 THz	broadband	Pulse
Photomixing	10 nW - 1 μ W	0.3 - 3 THz	continuous	CW
QCL	1 - 100 mW	1 - 5 THz	discrete lines	both

Table 1.1: Comparison of several kinds of THz sources

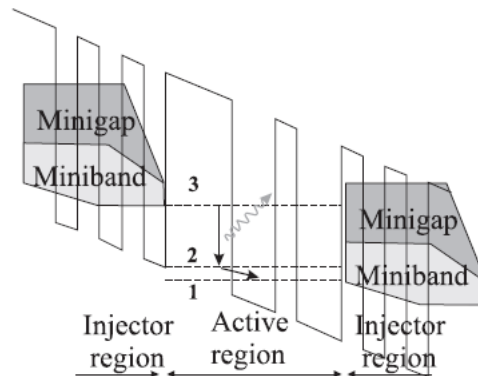


Figure 1.3: Schematic diagram of the conduction band structure of the quantum cascade laser. A THz photon with frequency $\nu = (E_3 - E_2)/h$ is generated. After Ref. [1].

1.3 THz detectors

Photoconductive antenna can be used also as a detector of THz radiation. The process is inverse: an optical ultrashort pulse generates free carriers in a semiconductor between electrodes of the antenna and they are accelerated by the electric field of simultaneously arriving THz pulse. This process generates a current which is converted to a voltage by a current amplifier connected to the antenna. The time resolution of the process is given by the length of the ultrashort optical pulse and by the response of the detector. The photocurrent J can be calculated from the transient photoconductivity σ and the THz electric field \mathcal{E}_{THz} in the photoconductor as $J(f) = \sigma(f)\mathcal{E}_{\text{THz}}(f)$ in frequency domain, or as a convolution in time domain $J(t) = \sigma(t) * \mathcal{E}_{\text{THz}}(t)$. To make the electric field approximately proportional to the photocurrent the photoconductivity response has to be much shorter than the THz waveform, i. e. $\sigma(f)$ has to be a flat function of f . Some suitable materials with such properties are radiation-damaged silicon-on-sapphire [6] and low-temperature-grown GaAs (LT-GaAs) [7]. LT-GaAs has a higher carrier mobility which leads to a stronger signal as is hence preferred.

Other technique of detection is the *electro-optic sampling* based on the linear electro-optic Pockels effect [8]. The birefringence of an electro-optic crystal is induced by the applied THz electric field and is probed by the gating optical pulse.

There are two basic configurations of the detecting system. In the first one (Fig. 1.4(a)), the circularly polarized gating beam passes through the crystal and the birefringence is then deduced from the ellipticity. The ellipticity

is measured as a difference signal from a pair of balanced photodiodes. The measured signal is linearly proportional to the THz field. This configuration is stable with respect to fluctuations of the gating beam polarization.

In the second configuration (Fig. 1.4(b)) the ellipticity is measured near the zero-

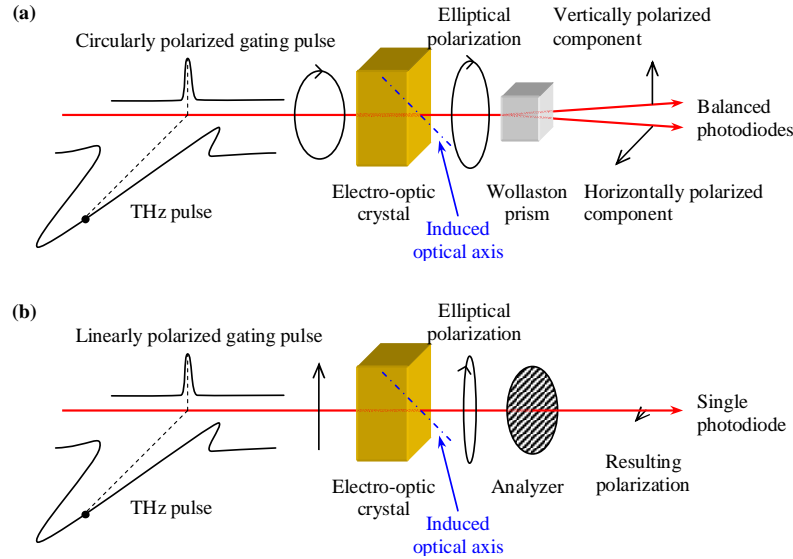


Figure 1.4: Basic schemes of electro-optic sampling systems. (a) Configuration employing a pair of balanced photodiodes. (b) Configuration operating near the zero-transmission point. After Ref. [9].

transmission point [10]. The detected signal becomes a non-linear function of the applied THz field. This scheme is important for a single-shot measurements [11] or in some imaging applications [12] where a single photodetector is required.

Often used crystals for electro-optic detection are ZnTe, DAST, LiTaO₃ or LiNbO₃ [13–15].

1.4 Time domain THz spectroscopy

THz time-domain spectroscopy provides a very useful tool for characterization of materials. It can be used to determine the optical constants in steady-state when a sample is in equilibrium as well as for investigation of dynamics.

The former can be done by steady-state spectroscopy. Time-domain THz *transmission* spectroscopy (TDTTS) is a standard method for characterization of the dielectric properties of a materials that are transparent in THz range like single crystals or thin films. We use this method in our experiments; the

experimental setup and the process of investigation is explained in the section 5.2.

When a sample is not transparent the time-domain THz *reflection* spectroscopy (TDTRS) can be used. The reflection spectroscopy may be useful also for investigation of thin films on substrates when the substrate is not suitable for the transmission measurement. The main difficulty of TDTRS is that a small mispositioning ($\sim 1\mu\text{m}$) of the sample with respect to the reference mirror significantly influences the calculated dielectric function due to a change in the reflectance phase [16].

The most common techniques for investigation of ultrafast dynamics (ultrafast photoconductivity) are optical pump-THz probe (OFTP) experiments and THz emission spectroscopy. In OFTP spectroscopy, the carrier dynamics photo-initiated by a pump pulse is probed by a delayed THz pulse [17]. The photo-induced response of the sample can be extracted from the time-dependent transient permittivity or conductivity. Since the energy of THz photons is low, OFTP spectroscopy is an excellent non-contact non-destructive electrical probe for various transport processes.

In the THz emission spectroscopy the THz pulses are emitted by the sample. The analysis of the THz signal gives the information about photoinitiated carrier dynamics in the sample. It is possible to examine evolution of carrier density and/or time-dependent carrier velocity [9].

1.5 Industrial applications

The THz radiation is interesting also for many industrial applications. THz radiation can penetrate through the materials like paper, clothing, ceramics, plastic, wood or masonry. Important applications are security checks [18]. For example airports can use THz radiation to uncover hidden weapons or dangerous substances under the clothes or in the luggage. THz rays allows also the ceramic knives to be uncovered that cannot be seen by metal detectors. Since a lot of chemical substances show fingerprints in THz spectral range, narcotics or explosives can be easy revealed [19], too.

THz radiation strongly interacts with water and therefore a skin cancer can be imaged by terahertz pulse imaging [20]. It is estimated that more than 85% of all cancers originate in the epithelium. THz radiation can be used to non-invasive molecular imaging of epithelial cancer. Moreover, the dentists can use THz instead of X-Rays to detect a decay at an early stage [21].

Another interesting application, which THz radiation is suitable for, is short-range wireless communication [22]. Most wireless gadgets use radiation

at microwave frequencies (Wi-Fi operates at 2.4 GHz). A typical modulator for a 2.4 GHz signal can only encode information at far lower frequencies, at about 50 MHz. But a 2.4 THz wave oscillates a thousand times faster than a 2.4 GHz signal, and correspondingly, if terahertz modulators could be made, the modulated signal would also be a thousand times faster.

Chapter 2

Metamaterials

2.1 Principles and historical overview

Metamaterials (MMs) are novel materials. In this chapter we will discuss metamaterials for electro-magnetic waves, although MMs approach goes beyond the optics, e. g. there have been done some works in acoustic MMs [23, 24].

The definition of metamaterial is still not absolutely clear, but after examining the key concepts behind MMs it can be said [25]: *”A metamaterial is an artificially structured material which attains its properties from the unit structure rather than the constituent materials. A metamaterial has an inhomogeneity scale that is much smaller than the wavelength of interest, and its electromagnetic response is expressed in terms of homogenized material parameters.”*

The structural units of a MM are known as meta-atoms or meta-molecules. Both meta-atoms and the average distance between neighboring meta-atoms must be substantially smaller than the target wavelength; usually we talk about MM when both are lower than $\lambda_0/10$, where λ_0 is the target wavelength in the vacuum. Often, but not always, MMs are periodical ordered materials. The light propagating through MM does not feel the microstructure; instead it feels an effective response. Thus we are able to set up the response and when creating an appropriate design, MMs can exhibit some optical properties that are not common in nature.

Going back to history we can say that the MM research was started in 1968 by Veselago [26], who theoretically considered the medium with a negative refractive index (NIM), i. e. $n < 0$. The Veselago’s question was: which sign for $n = \pm\sqrt{\epsilon\mu}$ is to be chosen when both ϵ and μ are equal to -1? For any realistic medium there is a positive imaginary part for ϵ and μ even small. This has to be in order to satisfy the causality condition. Considering $\epsilon = -1 + iq_1$ and

$\mu = -1 + iq_2$ where $0 < q_1, q_2 \ll -1$ we get

$$\begin{aligned} n &= \pm \sqrt{(-1 + iq_1)(-1 + iq_2)} = \pm \sqrt{(1 - q_1q_2) - i(q_1 + q_2)} \\ &\approx \pm \left[1 - i \frac{q_1 + q_2}{2} \right]. \end{aligned} \quad (2.1)$$

The causality requires also that the real part of n has to be positive and thus the minus sign has to be chosen. The negative real part of n implies that the phase velocity is opposite to the flow of energy. NIM are also known as the left-handed materials since the field vectors $\vec{\mathcal{E}}$, $\vec{\mathcal{H}}$ and the wave vector \vec{k} form a left-handed system for such media. This can be clear from Maxwell's equations for a plane wave,

$$\vec{k} \times \vec{\mathcal{E}} = \omega \mu_0 \mu \vec{\mathcal{H}} \quad (2.2a)$$

$$\vec{k} \times \vec{\mathcal{H}} = -\omega \epsilon_0 \epsilon \vec{\mathcal{E}} \quad (2.2b)$$

considering the fact that ϵ and μ are negative.

As Veselago showed, the idea itself brings very interesting new physical phenomena. The negative refractive index modifies the Snell's law for refraction on a interface between two media, $n_1 \sin \theta_i = n_2 \sin \theta_t$. If we consider the first medium with positive index $n_1 > 0$ and the second medium with negative index $n_2 < 0$, the angle of refraction θ_t has to be negative. The momentum conservation requests that at the interface of any two media the tangential component of the wave-vector must be continuous. Since the vector \vec{k} is oriented opposite to the Poynting vector, the ray coming from the positive index medium into NIM has to be refracted in a way showed in Fig. 2.1.

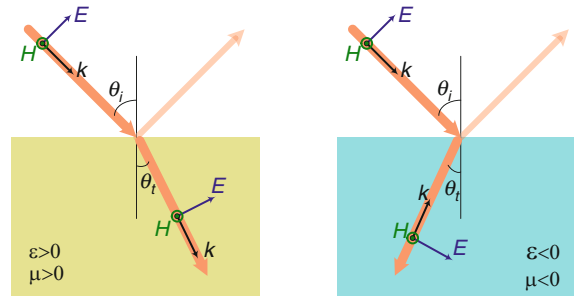


Figure 2.1: The refraction of ray coming from positive index medium to negative index medium. After Ref. [25].

Additionally, several other interesting fundamental effects such as reversed Doppler effect or reversed Cerenkov radiation were proposed in NIMs. Some of these has been already experimentally verified [27, 28].

Continuing in this work, Veselago predicted that using NIM it could be possible to prepare 'perfect lens', i. e. the lens with no dioptrical defects. In 2000, Pendry pointed out that a slab with negative refractive index $n = -1$ placed in vacuum beats the diffraction limit and allows imaging of objects with a sub-wavelength precisions [29]. This is because NIM has an unique property of amplifying evanescent waves. Evanescent waves are the waves with the transverse wave-vector $k_t = \sqrt{k_x^2 + k_y^2}$ that is higher than the wave-vector k_0 in free space. For these waves the wave-vector becomes imaginary and they decay exponentially in the propagation direction. Thus they do not have any contribution to the image obtained by standard lenses. Evanescent waves carry the information of sub-wavelength features of the object. Since the conventional imaging systems are unable to restore evanescent waves, they cannot provide a sub-wavelength resolution [30].

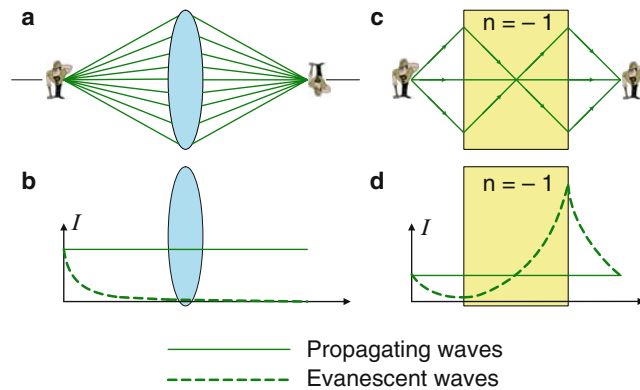


Figure 2.2: Comparison of the conventional lens and NIM slab lens. (a) A conventional lens only collects the propagating waves. (b) The loss of the evanescent waves in conventional imaging system. (c) The focusing ability of a NIM slab. (d) The growth of evanescent waves in the NIM slab and the restoration of both the propagating and evanescent waves. After Ref. [25].

Consider now a wave propagating in z -direction from an object. The field component of each Fourier mode from the object can be expressed as $\exp(-i\omega t + ik_z z)$. In free space, for propagating waves $k_z = \sqrt{k_0^2 - k_x^2 - k_y^2}$ is positive. For near-fields components we have $k_z = i\kappa_z = i\sqrt{k_x^2 + k_y^2 - k_0^2}$, where κ_z is a positive real number. According to the fact that k_z in NIM is with the negative sign, for evanescent waves we get $k_z = -i\kappa_z$. This leads to an exponential growth $\exp(\kappa_z z)$ of near-field components in NIM. We should notice that this fact does not violate energy conservation since the evanescent waves carry no energy.

First experiments on NIM structures were done by Smith et al. in 2000 [31],

where they presented work on structured materials with negative permittivity and simultaneously negative permeability at microwave frequencies. Year after, Shelby, Smith and Schultz published the experimental verification of a negative refractive index [32] at microwave frequencies, showing the modified Snell's law (see Fig. 2.3).

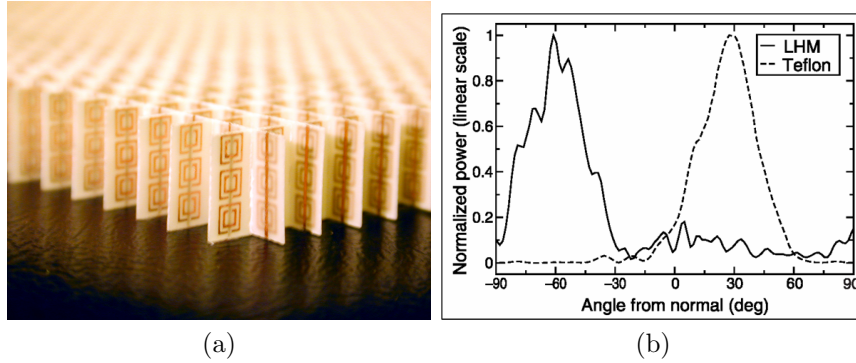


Figure 2.3: (a) The two-dimensional NIM at microwave frequency composed from wires and split rings. (b) The experimental result verified the modified Snell's law. After Ref. [32].

At the beginning of MMs research almost all of the works were connected with NIM and thus in the first years MM and NIM were almost synonyms. Nevertheless, nowadays approach goes far beyond NIM, although this is one of the biggest challenges of MMs research.

2.2 Metamaterial structures and effective response

The response of MM is crucially dependent on the architecture of meta-atoms. The theoretical description of metamaterial properties cannot be written in a simple way. The system of boundary conditions in such microstructures make Maxwell's equations practically impossible to be solved analytically. Nevertheless, under certain conditions the situation can be simplified. When studying the optical properties of a system composed of individual sub-wavelength particles, electromagnetic scattering is overshadowed by the average response of the whole structure and we can investigate the properties of microscopically heterogeneous composite by evaluating the *effective properties* of the macroscopically homogeneous medium.

Although the electric and magnetic response of MMs is considered to be

dependent on the structure of MM, we cannot forget that used materials play some role, too. It is clear that MMs made of dielectrics will exhibit different optical properties than MMs made from metals. The most of the MMs are composites of metals and dielectrics.

2.2.1 Quasi-static regime

Let us firstly consider some composite with sub-wavelength particles. In the quasi-static approximation, when the particles are substantially smaller than the wavelength of used electromagnetic radiation both in vacuum and in the components of the composite, the response does not show any additional resonances and we can express the field in the composite by some mean value. The sample can be described as an effective medium.

We will work with such samples later in this thesis, when we will try to compose the wave plates of an silicon substrates with etched metamaterial layers (see section 4.1).

The two of the most significant effective medium theories for such composites are the Maxwell-Garnett theory (MGT) [33] and the Bruggeman effective medium theory (EMT) [34]. In fact, EMT is an enhancement of MGT. The volume proportion of individual constituents in a composite is described by *filling factor* f .

Both theories consider a composite of two materials as a percolation of inclusions in the host medium. However, while in MGT one constituent represents the inclusions and the other represent the host medium, in EMT a single particle of any constituent is described as an inclusion in the whole structure that represents the host medium. In spite of EMT, when using of MGT we must say which component represents the inclusions and which component represent the host medium. Therefore MGT can be used only for well-percolated inclusions.

Considering the spherical inclusions the Bruggeman EMT expression reads [34]:

$$f_1 \frac{\epsilon_1 - \epsilon}{\epsilon_1 + 2\epsilon} + f_2 \frac{\epsilon_2 - \epsilon}{\epsilon_2 + 2\epsilon} = 0. \quad (2.3)$$

where $f_1, f_2, \epsilon_1, \epsilon_2$ are the filling factors and relative permittivities of first and second component, respectively, and ϵ is the effective permittivity of composite. This equation can be generalized to any number of components:

$$\sum_i f_i \frac{\epsilon_i - \epsilon}{\epsilon_i + 2\epsilon} = 0, \quad \sum_i f_i = 1. \quad (2.4)$$

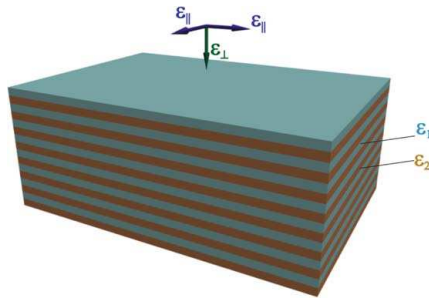


Figure 2.4: Scheme of a layered structure, with the permittivities of the two constituents given as ϵ_1 and ϵ_2 , respectively. Two principal effective permittivities are marked as ϵ_{\perp} and ϵ_{\parallel} . After Ref. [25].

As an advantage, EMT predicts a critical filling fraction for metal, which is usually referred to as the percolation threshold. For a three-dimensional metal-dielectric composite it corresponds to $f = 1/3$. Electronically, when $f < 1/3$, the composite acts as an insulator with an extremely low DC conductivity, and the composite becomes a conductor for $f > 1/3$ because there is formed a continuous metallic path across the sample and the metal component forms an infinite cluster [35].

When the shape of the inclusion particles is notably non-spherical, we must modify the form of EMT 2.3 by using a screening factor *kappa* that is related to the Lorentz depolarization factor L :

$$\kappa = (1 - L)/L. \quad (2.5)$$

The EMT formula then becomes [25]:

$$f_1 \frac{\epsilon_1 - \epsilon}{\epsilon_1 + \kappa\epsilon} + f_2 \frac{\epsilon_2 - \epsilon}{\epsilon_2 + \kappa\epsilon} = 0. \quad (2.6)$$

If the wavelength of used radiation in composite (not in free space) is comparable with the size of inclusions (i. e. the components exhibit high real permittivities or filling factor is above the percolation threshold), the resonances in electric and magnetic field can occurs. In these cases the EMT is not sufficient in determining the composite permittivity and permeability and numerical methods like multi-dimensional transfer matrix formalism [36] must be used to determine the effective response.

Nevertheless, EMT can be used for evaluating the permittivity of layered structure, when the thickness of the layers is below the wavelength (in the structure) as in Fig. 2.4. For i -th layer the flux density reads

$$\mathcal{D}_i = \epsilon_i \mathcal{E}. \quad (2.7)$$

When the incident wave is polarized parallel to the interfaces, the electric fields at boundaries of layers are continuous and thus same:

$$\mathcal{E}_1 = \mathcal{E}_2 = \mathcal{E}_{\text{eff}}. \quad (2.8)$$

The effective density flux of one pair of layers is volume averaged sum of density fluxes in individual constituents

$$\mathcal{D}_{\text{eff}} = f_1 \mathcal{D}_1 + f_2 \mathcal{D}_2 \quad (2.9)$$

and the effective permittivity reads

$$\epsilon_{\parallel} = f_1 \epsilon_1 + f_2 \epsilon_2. \quad (2.10)$$

On the other hand, for incident wave with polarization perpendicular to the interfaces of the layered structure the electric flux has to be continuous at the boundaries and so

$$\mathcal{D}_1 = \mathcal{D}_2 = \mathcal{D}_{\text{eff}}. \quad (2.11)$$

The electric field is weighted average of the individual fields,

$$\mathcal{E}_{\text{eff}} = f_1 \mathcal{E}_1 + f_2 \mathcal{E}_2 \quad (2.12)$$

From equations (2.7), (2.11), (2.12) we get effective permittivity

$$\epsilon_{\perp}^{-1} = f_1 \epsilon_1^{-1} + f_2 \epsilon_2^{-1}. \quad (2.13)$$

We should notice two things. First, equations (2.10), (2.13) are the equations for the permittivity of parallel and serial condensators, respectively. However this computation could be done only in quasi-static approximation. Second, equations (2.10) and (2.13) can be achieved from (2.6) as two extremes: when $\kappa \rightarrow \infty$, it corresponds with zero screening and ϵ_{\parallel} ; when $\kappa = 0$, it corresponds with full screening and ϵ_{\perp} .

2.2.2 Metamaterial resonances

At higher frequencies resonances of electric and magnetic response occurs in MMs due to the geometry of the pattern. For example, inside a dielectric MM, the wavelength is comparable to the dimension of the meta-atom and so called Mie resonances occur which may be observed either in ϵ or in μ or in both [48].

Let now focus on metal MMs. One way to reach negative ϵ is using a rodged metal media by W. Rotman [37], see Fig. 2.5. Such a medium is designed to produce a plasma resonances. The plasma frequency of wire array depends

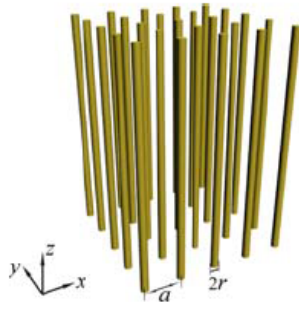


Figure 2.5: 2-dimensional array of rodded media for z -polarized field. After Ref. [25].

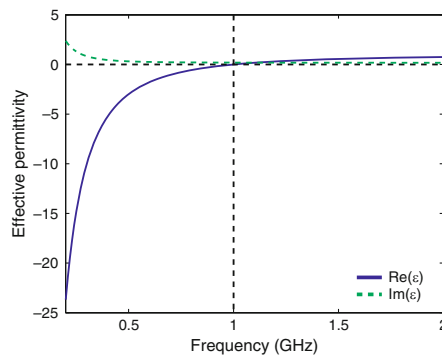


Figure 2.6: The dielectric function of a silver wire array with $r = 5 \mu\text{m}$ and $a = 40 \text{ mm}$. The horizontal axis represents the wave frequency $f = \omega/2\pi$. The effective plasma frequency is $\omega_p = 2\pi \times 1 \text{ GHz}$. After Ref. [25].

mostly on the geometrical properties of wires, i. e. diameter $2r$ and the length of the unit cell a . It can be shown [25] that the plasma frequency ω_p reads:

$$\omega_p^2 = \frac{2\pi c^2}{a^2 \ln(a/r)}, \quad (2.14)$$

where c is the speed of light in vacuum. The effective permittivity of wire medium can be written in Drude form:

$$\epsilon_{\text{eff}}(\omega) = 1 - \frac{\omega_p^2}{\omega(\omega + i\epsilon_0 a^2 \omega_p^2 / \pi r^2 \sigma)}, \quad (2.15)$$

where ϵ_0 is the vacuum permittivity and σ is the conductivity of the used metal. One example of the permittivity for such media with plasma frequency in GHz range is in Fig. 2.6.

While the permittivity of metals is usually negative under the plasma frequency, the magnetic permeability is in optics usually close to its free space

value. However, there have been works on challenging magnetic response of artificial structures. Pendry et al. [38] predicted, that the pair of split ring resonators (SRRs) with subwavelength dimensions can lead to a non-unity effective permeability

$$\mu_{\text{eff}} = 1 - \frac{\pi r^2 / a^2}{1 - 3l / \pi^2 \mu_0 \omega^2 C r^3 + i(2l\rho / \omega r \mu_0)}, \quad (2.16)$$

where ρ is the resistance per unit length of the rings measured around the circumference, ω is the frequency of incident radiation, l is the distance between layers, a is the lattice parameter, r is internal radius of internal split ring (see Fig. 2.7).

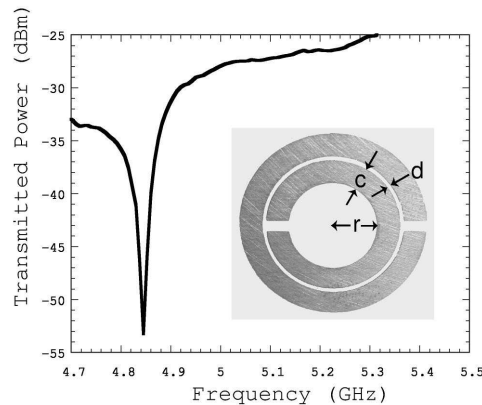


Figure 2.7: Resonance curve of an actual copper split ring resonator. $c = 0.8$ mm, $d = 0.2$ mm, $r = 1.5$ mm. The SRR has its resonance at about 4.8 GHz. After Ref. [31].

In fact, the NIM for GHz range that Shelby [32] used for an experimental achieving of negative refractive index was a combination of the wire medium together with the SRRs (see Fig. 2.3).

Use of metal wires and SRRs is not the only option for NIMs, neither for MM concept. In fact, NIMs based on electric and magnetic resonances are not promising since the system is lossy and plasmonic resonance frequency for electric and magnetic field can overlap. The most promising structure, especially at optical frequencies, is 'fishnet' structure (see Fig. 2.8) [39]. There are several other MM structures with magnetic response at THz frequencies, such as staple-shaped nanostructures [40] or single planar SRR structure [41].

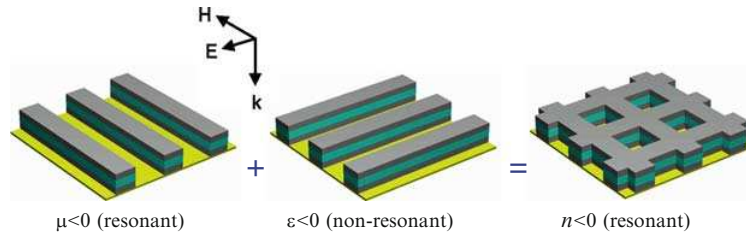


Figure 2.8: The fishnet structure: resonant magnetic strips combined with a non-resonant electric grating. After Ref. [25].

2.3 Applications

As mentioned in the first section, one of the interesting applications of MMs is creation of perfect lens. Unfortunately, the NIMs based on resonances are highly dissipative, lossy and anisotropic and thus practically do not make the perfect lens. The near-field version of the perfect lens, 'near-field superlens', does not require optical magnetism and is easier to achieve. Such lens should be used in biomedical imaging (surface-enhanced Raman scattering, near-field scanning optical microscopy) or nanolithography. There is also an effort to create far-field superlens [42, 43].

The other possibility of big interest is using MMs in transformation optics. Transformation optic proposed several conceptual devices of a big interest such as hyperlens or cloaking devices. The brief overview can be found in [44].

The idea of cloaking device is in designing an optical element that transforms path of light so it will go around the object which we want to hide. It is somehow interesting that the Maxwell's equations are form-invariant under a space-deforming transformation. The strategy of cloaking device is based on a such coordinate transformation. In the first step, we apply a form-invariant transformation to Maxwell's equations in the real space with emphasis on required functionality. Then we transform the permittivity and permeability tensors back to the real space and fabricate resulting medium. Considering the fact that permittivity and permeability tensor will be very complicated it is clear that such medium is difficult to prepare, although experimental demonstrations at microwave frequencies were done [45].

Going beyond the NIM, MMs can be used to construct some devices operating at designated frequencies, like switches, modulators or detectors. Such structures are especially important for THz spectral range since many common materials do not respond to THz radiation at all. As mentioned in the previous chapter, THz radiation has huge application potential and therefore MM structures for THz range are in a big interest of researchers. In 2006, H.-T. Chen

et al. proposed [46] active THz device consisted of an array of gold electric resonator elements (the metamaterial) connected by wires and fabricated on a semiconductor substrate (*n*-GaAs). The substrate and metamaterial array effectively formed together a Schottky diode which enable the modulation of THz transmission by 50% using a reverse gate voltage bias. Thus this structure can serve as an electrical modulator for THz frequencies.

Later Chen et al. showed, that by using a similar geometry of resonator array fabricated on ErAs/GaAs nanoisland superlattice substrates it is possible to create an ultrafast optical switch for THz radiation with a recovery rate of ~ 10 ps [47].

Some terahertz metamaterials can be tuned also by temperature. In 2009 Němec et al. presented [48] dielectric metamaterials exhibiting a tunable range of negative effective permeability in the terahertz spectral region. The structures consisted of arrays of intrinsically nonmagnetic rods made of an incipient ferroelectric SrTiO₃ which a high tunable permittivity by temperature control.

Chapter 3

Polarization of light

3.1 Polarization of light

The light is an electromagnetic wave. The polarization of light is determined by the time course of the direction of the electric vector $\vec{\mathcal{E}}(\vec{r}, t)$. For monochromatic light, at each position \vec{r} the endpoint of the vector $\vec{\mathcal{E}}(\vec{r}, t)$ moves in a plane and traces an ellipse, but the plane, the orientation and the shape of the ellipse generally vary with position. However, in paraxial optics, if the medium is isotropic, the polarization ellipse is approximately the same everywhere and the wave is said to be elliptically polarized.

Consider monochromatic plane wave of frequency ν traveling in the z direction with velocity c . The electric field lies in the $x - y$ plane and is generally described by

$$\vec{\mathcal{E}}(z, t) = \text{Re} \left\{ \vec{A} \exp \left[j2\pi\nu \left(t - \frac{z}{c} \right) \right] \right\}. \quad (3.1)$$

Here the complex envelope

$$\vec{A} = A_x \vec{x} + A_y \vec{y} \quad (3.2)$$

is a vector with complex components A_x, A_y . These components can be expressed in terms of their magnitudes and phases,

$$A_x = a_x \exp(j\phi_x), \quad (3.3a)$$

$$A_y = a_y \exp(j\phi_y). \quad (3.3b)$$

Substituting (3.2) and (3.3) into (3.1), we obtain

$$\vec{\mathcal{E}}(z, t) = \mathcal{E}_x \vec{x} + \mathcal{E}_y \vec{y}, \quad (3.4)$$

where the x and y components of the vector $\vec{\mathcal{E}}$ are

$$\mathcal{E}_x = a_x \cos \left[2\pi\nu \left(t - \frac{z}{c} \right) + \phi_x \right] \quad (3.5a)$$

$$\mathcal{E}_y = a_y \cos \left[2\pi\nu \left(t - \frac{z}{c} \right) + \phi_y \right] \quad (3.5b)$$

Equations (3.5) are the parametric equations of the ellipse

$$\frac{\mathcal{E}_x}{a_x^2} + \frac{\mathcal{E}_y}{a_y^2} - 2 \cos \phi \frac{\mathcal{E}_x \mathcal{E}_y}{a_x a_y} = \sin^2 \phi, \quad (3.6)$$

where $\phi = \phi_x - \phi_y$ is the phase difference, also called the relative phase. The shape of the ellipse determines the state of polarization and depends on two parameters: the ratio of magnitudes a_x/a_y and the phase difference $\phi = \phi_y - \phi_x$. The light is right polarized if $\sin \phi > 0$ and left polarized if $\sin \phi < 0$. To describe polarization we may implement new parameters χ (ellipticity), ψ (angle of rotation) and α (see fig. 3.1), where:

$$\tan 2\psi = \frac{2a_x a_y \cos \phi}{a_x^2 - a_y^2} \quad (0 \leq \psi \leq \pi), \quad (3.7a)$$

$$\tan \alpha = \frac{a_y}{a_x} \quad (0 \leq \alpha \leq \pi/2), \quad (3.7b)$$

$$\tan \chi = \operatorname{sgn}[\sin \phi] \frac{b}{a} \quad (-\pi/4 \leq \chi \leq \pi/4) \quad (3.7c)$$

where a and b are ellipse's semimajor and semiminor axes, respectively. For us

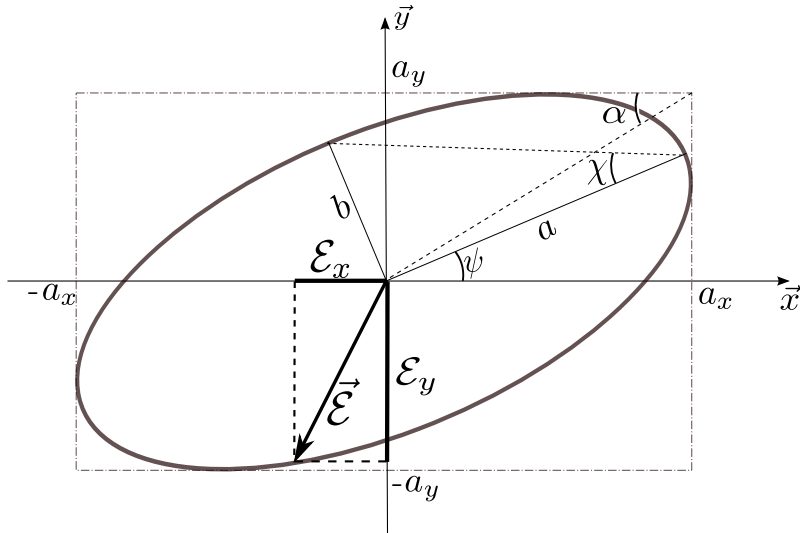


Figure 3.1: Ellipse of polarization

there are two interesting states of polarization, *linear* and *circular*.

Light is *LINEARLY POLARIZED* if one of the components vanishes ($a_x = 0$ or $a_y = 0$) or $\sin \phi = 0$, i. e. $\phi = k\pi$, k is an integer. Ellipse is reduced to a line, $\chi = 0$.

Light is *CIRCULARLY POLARIZED* if $a_x = a_y$ and $\phi = \pm\pi/2$ ('+' for right circularly polarized and '-' for left circularly polarized). Ellipse is reduced to a circle, $\chi = \pi/4$.

3.2 Jones-vector representation

Complex envelopes A_x, A_y completely characterize a monochromatic plane wave traveling in z direction. Since they represent orthogonal components, they can be written in the form of a column matrix known as the *Jones vector*

$$J = \begin{bmatrix} A_x \\ A_y \end{bmatrix} \quad (3.8)$$

Some states of polarization expressed as Jones vectors are shown in table 3.1.

Linearly polarized wave in x direction	$\begin{bmatrix} 1 \\ 0 \end{bmatrix}$
Linearly polarized wave in y direction	$\begin{bmatrix} 0 \\ 1 \end{bmatrix}$
Linearly polarized wave with plane of polarization making angle δ with x axis	$\begin{bmatrix} \cos \delta \\ \sin \delta \end{bmatrix}$
Right circularly polarized wave	$\frac{1}{\sqrt{2}} \begin{bmatrix} 1 \\ j \end{bmatrix}$
Left circularly polarized wave	$\frac{1}{\sqrt{2}} \begin{bmatrix} 1 \\ -j \end{bmatrix}$

Table 3.1: Jones vectors

Polarization device or another optical system can be expressed as the *Jones matrix*, T . Jones matrix is a 2x2 matrix that transforms input wave $J_1 = \begin{bmatrix} A_{1x} \\ A_{1y} \end{bmatrix}$

to output wave $J_2 = \begin{bmatrix} A_{2x} \\ A_{2y} \end{bmatrix}$ as

$$\begin{bmatrix} A_{2x} \\ A_{2y} \end{bmatrix} = \begin{bmatrix} T_{11} & T_{12} \\ T_{21} & T_{22} \end{bmatrix} \begin{bmatrix} A_{1x} \\ A_{1y} \end{bmatrix} \quad (3.9)$$

The *normal modes* of polarization system are the states of polarization that are not changed by the system, i. e. satisfying condition

$$TJ = \gamma J, \quad (3.10)$$

where γ is a constant.

3.3 Wave retarders

Wave retarders are optical devices able to change relative phase ϕ of the incident wave. The change of polarization is caused by a birefringence of the wave retarder. In general, a wave retarder has two *normal modes*, linearly polarized waves in x and y direction (called fast and slow axes of the retarder, respectively). At the beginning, an incident wave is decomposed to these normal modes, then each component propagate independently and finally these components are recomposed into an output wave (see fig. 3.2). Since a wave plate is birefringent, each mode travels different optical path length. This leads to a different phase shift of each component and thus to a change of relative phase. A wave retarder can be described in Jones-vector representation as a matrix

$$T = \begin{bmatrix} 1 & 0 \\ 0 & \exp(-j\Gamma) \end{bmatrix} \quad (3.11)$$

where Γ is a relative phase change.

3.3.1 Half-wave plate

In case of $\Gamma = \pi$, the retarder is called half-wave retarder or half-wave plate. Substituting Γ into (3.11) one can easily get Jones matrix of half-wave plate $T_{1/2}$

$$T_{1/2} = \begin{bmatrix} 1 & 0 \\ 0 & -1 \end{bmatrix}. \quad (3.12)$$

Half-wave plate converts linearly polarized light $\begin{bmatrix} \cos \delta \\ \sin \delta \end{bmatrix}$ into linearly polarized light $\begin{bmatrix} \cos(-\delta) \\ \sin(-\delta) \end{bmatrix}$, i. e. rotates plane of linearly polarized wave from angle δ to angle $-\delta$ (see fig. 3.2). The half-wave plate also converts right circularly polarized light $\begin{bmatrix} 1 \\ j \end{bmatrix}$ into left circularly polarized light $\begin{bmatrix} 1 \\ -j \end{bmatrix}$ and reversely.

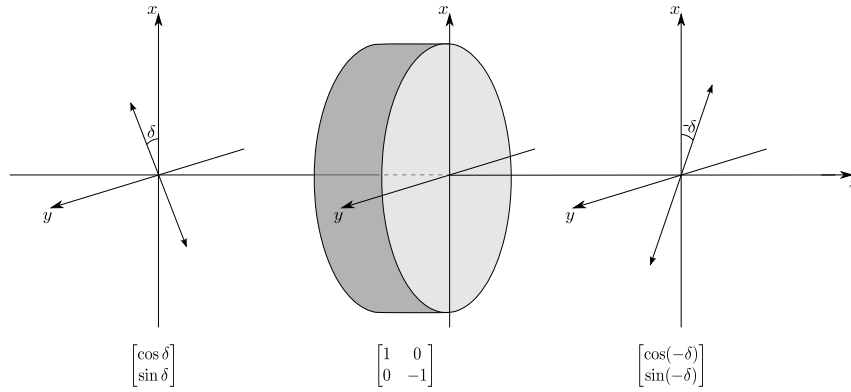


Figure 3.2: Linearly polarized wave passing through a half-wave plate. Half-wave plate rotates plane of polarization.

3.3.2 Quarter-wave plate

In case of $\Gamma = \pi/2$, the retarder is called quarter-wave retarder or quarter-wave plate. Substituting Γ into (3.11) one can easily get Jones matrix of quarter-wave plate $T_{1/4}$

$$T_{1/4} = \begin{bmatrix} 1 & 0 \\ 0 & -j \end{bmatrix}. \quad (3.13)$$

Quarter-wave plate converts linearly polarized light $\begin{bmatrix} 1 \\ 1 \end{bmatrix}$ ($\delta = 45^\circ$) into left circularly polarized light $\begin{bmatrix} 1 \\ -j \end{bmatrix}$, and reversely, right circularly polarized light $\begin{bmatrix} 1 \\ j \end{bmatrix}$ into linearly polarized light $\begin{bmatrix} 1 \\ 1 \end{bmatrix}$. Further, one can easily see that

$$T_{1/4}T_{1/4} = T_{1/2}, \quad (3.14)$$

and thus a system composed of two quarter-wave plates with same fast and slow axis behave as a system composed of a half-wave plate.

Chapter 4

Wave plates

The aim of the work was to develop quarter-wave plate and half-wave plate working in THz range. The idea was to design such device by using anisotropic metamaterial layers made of silicon and optimize its transmission using transfer matrix formalism.

4.1 Etched layers for THz radiation

Based on recent work of Kadlec et al. [49], strongly birefringent metamaterials in THz range can be prepared by etching of patterns with appropriate filling factors in a dielectric substrate. The idea is simple and fresh, by deep etching of subwavelength periodic parallel lines (walls) we create metamaterial with chosen refractive indices for two orthogonal light polarizations: along the walls and perpendicular to the walls. By etching another set of lines perpendicular to the first set one obtains an additional degree of freedom to define the values of refractive indices. If a structure filling factor is same in both directions, we can create an isotropic metamaterial layer with refractive index of any value between 1 (air) and the substrate refractive index. Such layer looks like a 2-dimensional grid of pillars, see fig. 4.1(c). When the dimensions of the unit cell (fig. 4.1(a)) are much smaller than the target wavelength (typically $\leq \lambda/10$), the structure can be described by effective permittivity values. Within the quasi-static approximation, the unit cell can be replaced by an equivalent electrical circuit (fig. 4.1(b)) that simplifies calculations of effective permittivities $\epsilon_{1,2}$ for two orthogonal linear polarizations. As a result we get [49]:

$$\vec{\mathcal{E}} \perp x_1 : \quad \epsilon_1 = 1 + \frac{x_1 x_2}{\frac{\epsilon}{\epsilon-1} - x_2} \equiv n_1^2 \quad (4.1a)$$

$$\vec{\mathcal{E}} \perp x_2 : \quad \epsilon_2 = 1 + \frac{x_1 x_2}{\frac{\epsilon}{\epsilon-1} - x_1} \equiv n_2^2 \quad (4.1b)$$

where ϵ is the material permittivity (i. e. ϵ_{Si} for silicon) and x_1 and x_2 denotes filling factors (fig. 4.1(a)), i. e. material and vacuum proportion within a period. These two linear polarizations represent normal modes of the layer. If filling factors x_1 and x_2 are different from each other, effective permittivities $\epsilon_{1,2}$ are different from each other as well. This leads to effective anisotropic optical (THz) properties of such layer.

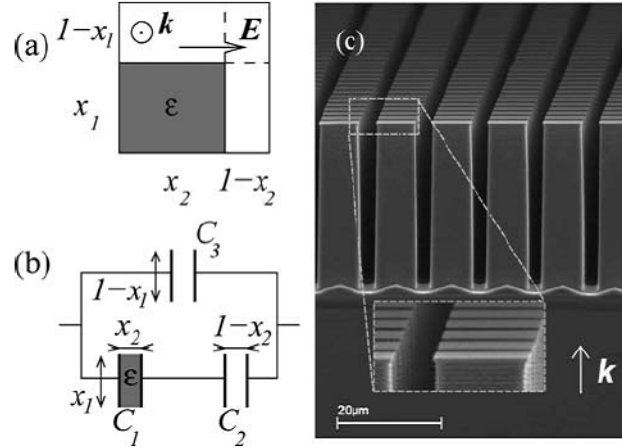


Figure 4.1: (a) Scheme of a unit cell of an etched material with permittivity ϵ placed in air; (b) equivalent circuit applicable for evaluating its effective response. The dimensions are in relative units. (c) Scanning electron microscope picture of the structure with an array of pillars. After Ref. [49].

Special case of etched layers are layers etched in one direction, i. e. $x_1 = 1$, $x_2 = x < 1$. Such layers are composed of walls separated by vacuum. This leads to a higher birefringence than in structures with an array of pillars. The birefringence amounts up to $\Delta n = 1.25$ for the filling factor $x = 0.65$ when using Si as a substrate [49]. Equations (4.1a), (4.1b) are simplified:

$$\vec{\mathcal{E}}_s \equiv \vec{\mathcal{E}} \perp x_1 : \quad \epsilon_s = \frac{\epsilon}{\epsilon - x(\epsilon - 1)} = n_s^2 \quad (4.2a)$$

$$\vec{\mathcal{E}}_p \equiv \vec{\mathcal{E}} \perp x_2 : \quad \epsilon_p = 1 + x(\epsilon - 1) = n_p^2 \quad (4.2b)$$

where we used 's' and 'p' indices instead of '1' and '2' since these indices intuitively indicate, within the usual optical convention, the polarization of light with respect to the wall direction. Equations (4.2a) and (4.2b) recall the expressions for serial (s) and parallel (p) capacitors, respectively (compare with equations (2.10), (2.13)). As a rule, $n_s < n_p$ because for serial capacitors the low-permittivity layer (air) substantially decreases the effective permittivity of the composite (so called "dead layers" in the literature).

4.2 Design of a wave plate

To obtain a wave-retarder we need to set the correct phase delay between eigenmodes $\mathcal{E}_p, \mathcal{E}_s$ and to achieve the same transmittance for these modes. First, let us consider dielectric etched walls on a dielectric substrate (fig. 4.2).

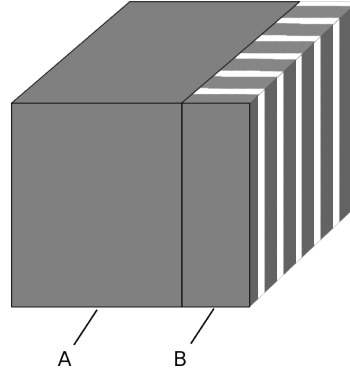


Figure 4.2: Scheme of a sample with etched walls. Part A is a bulk material, part B is an etched material.

The sample comprises three interfaces: air/substrate, substrate/etched-layer, etched-layer/air. The first interface exhibits a high reflectance due to the high impedance mismatch between the air and the material. To increase the transmittance we can add an antireflective layer for the substrate. The antireflective layer can be designed as another etched-layer with appropriately chosen refractive index and thickness. This layer will be isotropic ($x_1=x_2$). Also we can try to avoid losses on etched-layer/air interface by using another birefringent etched-layer. As we will see later, it will not be perfectly antireflective, but with this layer we will be able to reach transmittance almost 100%. This layer also comes along with a new substrate, so we will need to add another antireflective layer for the substrate. The final design of wave plate can be splitted into 5 parts: A, B, C, D, E (see fig 4.3). We will give a detailed look into each part in the next subsections.

4.2.1 Layer C

Layer C is an isotropic etched layer that behaves like a single-layer antireflective coating. As mentioned above, it is used to increase the absolute transmittance of the wave plate and to suppress the Fabry-Perot interference of the whole structure. For a given frequency f_0 , the layer is antireflective if it satisfies two conditions [50]:

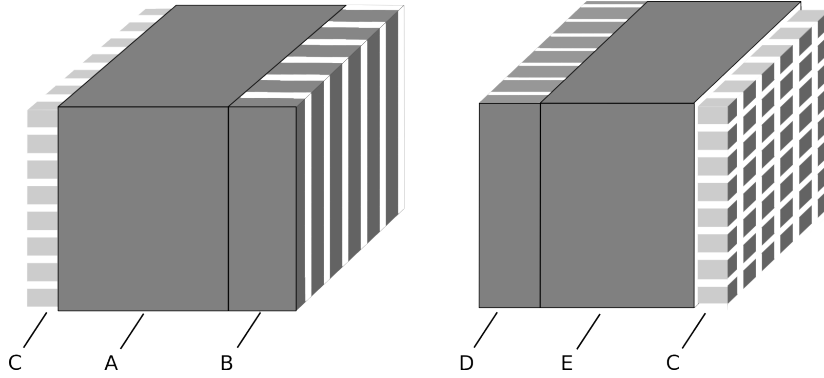


Figure 4.3: Scheme of a wave plate. A,E - bulk material, B,D - etched walls, C - antireflective layer (isotropic etched pillars). In experiment there will be no space between B and D.

1. refractive index of the layer n_{arl}

$$n_{arl} = \sqrt{n_i n_o}, \quad (4.3a)$$

2. thickness of the layer d_{arl} :

$$d_{arl} = \frac{\lambda_0 (2m + 1)}{4n_{arl}}; \quad m \in \{0, 1, 2, \dots\}, \quad (4.3b)$$

where n_i and n_o are the refractive of media above and below the layer, respectively, λ_0 is the wavelength of radiation in vacuum, $\lambda_0 = c/f_0$, where c is the speed of light in vacuum. Since $n_i = 1$ (air) and $n_o = 3.415$ (Si) we found that refractive index of layer C is

$$n_c = \sqrt{3.42} \approx 1.85.$$

Using (4.1a) and (4.1b) we find the appropriate filling factors $x_{c1} = x_{c2} = 0.815$. The depth of etching is given by (4.3b). By using Occam's razor we find that $m = 0$ and

$$d_c = 40.5 \mu\text{m} \quad \text{for } 0.5 \text{ THz}$$

$$d_c = 81.0 \mu\text{m} \quad \text{for } 1 \text{ THz}.$$

4.2.2 Layers A and E

Layers A and E are substrate layers (bulks of Si that hold the etched layers). In fact, each of them is composed of two substrates: one substrate holds the layer C and the other holds the layer B or D. This is because a structure etched from

both sides is more difficult to prepare than a substrate etched from one side. Experimentally we need to eliminate the air layer between these two substrates to obtain an optically homogeneous thicker substrate.

Since the layer C suppresses Fabry-Perot interference, we do not need to optimize thicknesses of layers A and E. Nevertheless, we assume that substrates will be 200-300 μm thick, therefore layer A and layer E will be approximately 500 μm thick.

4.2.3 Layers B and D

Layers B and D are both anisotropic and thus are birefringent. Thinner layers are easier to prepare than thicker ones so we will not discuss a deeper etching than necessary. Our target frequency is about 1 THz ($\lambda_0 = 300 \mu\text{m}$); the size of the unit cell of the etched pattern should not then exceed $a = 30 \mu\text{m}$ in order to satisfy the condition $a \leq \lambda_0/10$. From the technological point of view the walls should be separated by at least a few microns (3-5 μm). Therefore the filling factors will never exceed 0.9. Further, the depth of etching should not exceed approximately 100 μm .

In fact, without a D layer there is nothing to optimize as the B layer must ensure alone the correct phase delay. In this case the reflection losses on A/B and B/air interfaces will differ for 's' and 'p', which means that the transmittance of the whole wave plate for these two polarizations will differ, too.

Below we show that using 2 birefringent layers provides sufficient degree of flexibility to optimize the design. The phase retardation of a wave plate is a sum of partial contributions, i. e.

$$\Delta\phi = \Delta\phi_b + \Delta\phi_d = \frac{2\pi d_b (n_{bp} - n_{bs})}{\lambda_0} + \frac{2\pi d_d (n_{dp} - n_{ds})}{\lambda_0}. \quad (4.4)$$

B and D layer should have equal orientations of slow and fast axes. If not, the phase retardation of B layer goes against the phase retardation of D layer. First, let us assume the layer D defines some phase delay and serves at the same time as an antireflective layer between B and silicon E. Since we prefer thinner layers rather than thicker, we will assume that layer B shows the highest possible birefringence, 1.25, i. e. filling factor $x_b = 0.65$. Thus the refraction indices of B are $n_{bs} = 1.57$ and $n_{bp} = 2.82$ and by satisfying condition (4.3a) we can find that refraction indices of D are $n_{dp} = 3.10$ and $n_{ds} = 2.32$ with corresponding filling factors $x_{d1} = 0.99$ and $x_{d2} = 0.89$. We are unable to etch layer with filling factor equal to 0.99, but instead we can prepare a layer with $x_{d1} = 1$ by etching walls instead of pillars. This leads to a little mismatch in n_{dp} and n_{ds} , but it is not critical ($n_{dp} = 3.24$ instead of 3.10, mismatch in n_{ds} is lower than 0.01).

A more serious problem in this case comes from a high predicted value of the D-layer thickness (substantially higher than $100 \mu\text{m}$). Since we have to accomplish the condition (4.3b) for both polarizations simultaneously, we find that the lowest acceptable thickness is $d_d \approx 161 \mu\text{m}$ for $f_0 = 1 \text{ THz}$. Even though we reach theoretical filling factors and depths, losses still remain because of the reflection on A/B interface.

Instead of making D antireflective we will follow an optimization procedure in order to reach the same transmission close to 100%.

4.3 Optimization of transmission

Our plan is to develop quarter-wave plate operating at target frequencies $f_0 = 0.5 \text{ THz}$ and $f_0 = 1 \text{ THz}$. Additionally, we can make a half-wave plate working on frequency $f_0 = 1 \text{ THz}$ just by appropriately changing the antireflective C layers in a quarter-wave plate designed for $f_0 = 0.5 \text{ THz}$. The optimization of transmission is done by preparing appropriate script (defining the optical and geometrical properties of the target structures) for the computer software developed by Petr Kužel and his colleagues at the Laboratory of Terahertz Spectroscopy. The software uses transfer matrix formalism described below.

4.3.1 Transfer matrix formalism

The optical properties of layered structures can be described by the transfer matrix formalism [51, 52]. The transfer matrices relate the tangential components of the electric \mathcal{E} and magnetic \mathcal{H} field at input and output interfaces, i. e.

$$\begin{bmatrix} \mathcal{E}_{in} \\ \eta_0 \mathcal{H}_{in} \end{bmatrix} = M \begin{bmatrix} \mathcal{E}_{out} \\ \eta_0 \mathcal{H}_{out} \end{bmatrix}, \quad (4.5)$$

where M is the appropriate transfer matrix and $\eta_0 = \sqrt{\mu_0/\epsilon_0}$ is the vacuum impedance. For the case of the normal incidence, the transfer matrix of a single dielectric homogeneous layer reads:

$$S = \begin{bmatrix} \cos(nk_0d) & i/n \sin(nk_0d) \\ in \sin(nk_0d) & \cos(nk_0d) \end{bmatrix}, \quad (4.6)$$

where n is the complex refractive index of the layer, d is the thickness of the layer and $k_0 = \omega/c$ is the wave vector in vacuum. The field distribution in the layer can be expressed as

$$\mathcal{E}(\omega, z) = \mathcal{E}_{in}(\omega) \cos(nk_0z) - i \frac{\eta_0 \mathcal{H}_{in}(\omega)}{n} \sin(nk_0z), \quad (4.7)$$

with $0 \leq z \leq d$.

The transfer matrix of the whole multi-layer stack equals the product of the transfer matrices of all constituents. For any general layered structure surrounded by air the amplitude transmission t and reflection r coefficients read

$$t = \frac{2}{m_{11} + m_{12} + m_{21} + m_{22}}, \quad (4.8a)$$

$$r = \frac{m_{11} + m_{12} - m_{21} - m_{22}}{m_{11} + m_{12} + m_{21} + m_{22}}, \quad (4.8b)$$

where m_{ij} are the components of transfer matrix of the structure.

4.3.2 Optimization results

Finally, we have found optimal parameters of each layer of quarter-wave plates on target frequencies 0.5 THz and 1 THz, see Tab. 4.1. Using these parameters we computed theoretical values transmissions for 's' and 'p' polarizations, relative transmission and phase retardation of each considered wave plate. Rather than in this section we prefer to show this data in the next chapter in the contrast to the experimental results.

f_0 [THz]	C			B		D	
	d_c [μm]	x_{c1}	x_{c2}	d_b [μm]	x_b	d_d [μm]	x_d
0.5	81.0	0.82	0.82	20.0	0.75	119.0	0.85
1	40.5					46.6	

Table 4.1: Optimized parameters of etched layers

Our idea was to make design as simple as possible and thus we have used one type of layer B for both wave plates. On the other hand this implies high depth of etching of layer D for $f_0 = 0.5$ THz.

For theoretical calculations the filling factor is considered as a parameter but for manufacturing we have to define the period of etching a and the width of etched lines (space) s or the width of etched walls (Si) w , see fig. 5.3. Lines must be at least $s = 4 - 5 \mu\text{m}$ wide and they can be prepared with $\sim 1 \mu\text{m}$ precision due to the technological limits.

As we have mentioned before, to consider a layer as a metamaterial the period of etching a should not exceed $\sim 30 \mu\text{m}$. Besides, simulations using 3D transfer matrix (3DTM) formalism [9] show that for $a > 20 \mu\text{m}$ an increase of n_s occurs at higher frequencies within our experimentally accessible spectral range. It means that for $f_0 = 1$ THz and $x = 0.85$ an increase of period

$\Delta a = 6.7 \mu\text{m}$ corresponds to an increase of refractive index $\Delta n_s = 0.04$ (see fig. 4.4). A small increase of the refractive index for 'p' polarization also occurs, but it is much lower than for 's' polarization.

In figure 4.4 we also show the static value of refractive indices calculated using (4.2a) and (4.2b). The static value of the permittivity calculated by 3DTM formalism depends on the discretization of space (distance between the mesh points where the permittivity and fields are evaluated). Especially ϵ_s depends on this factor. This is observed in fig. 4.4 as a small increase of n_s calculated by 3DTM compared to the static value evaluated through (4.2a).

Considering this we proposed to decrease the aimed values of filling factors (and thus the refractive indices) appropriately. Due to high filling factors, layers C are designed with a large period $a = 27 \mu\text{m}$. The target width of etched lines is $s = 5 \mu\text{m}$, so filling factor $x_c = 22/27 = 0.815$.

Layer D has even higher filling factor than the layer C; to reach the desired refractive indices we need to etch lines that are $s = 5 \mu\text{m}$ wide with period a between $28 \mu\text{m}$ and $30 \mu\text{m}$. Because layer D is deep enough close to the upper technological limit, we try to etch lines with $a = 28 \mu\text{m}$ and $a = 30 \mu\text{m}$ and then pick better one.

Layer B is designed with etched lines $s = 4 \mu\text{m}$ wide and period $a = 15 \mu\text{m}$ (instead of the theoretical one of $16 \mu\text{m}$ which would imply $x_b = 0.75$).

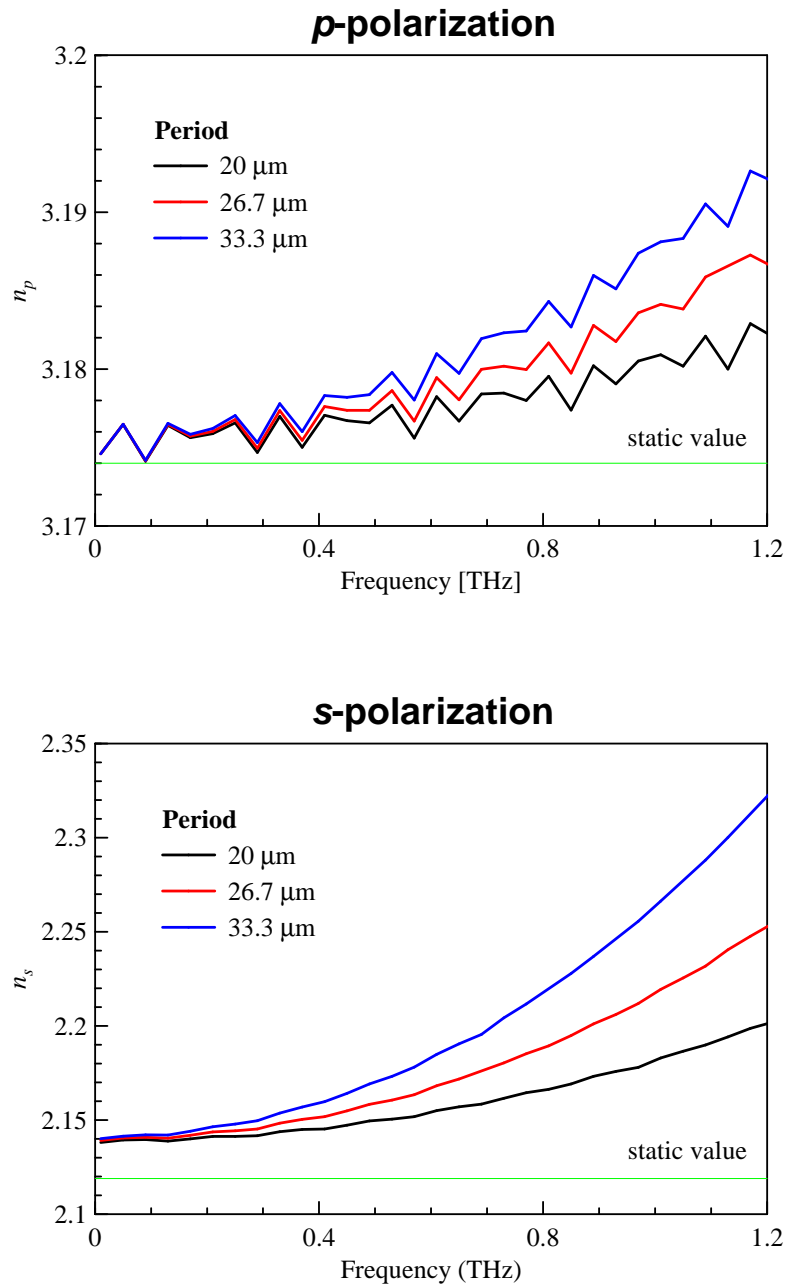


Figure 4.4: Computation of refractive indices n_p , n_s using 3D transfer matrix formalism.

Chapter 5

Experiments and results

Characterization of samples and wave plates was done by THz time-domain spectroscopy in transmission geometry.

5.1 Experimental setup

For a detailed look into our experimental arrangement see figure 5.1. Our laser system consists of the Coherent Mira Seed femtosecond oscillator pumped by the Coherent Verdi pumping laser. Verdi is a solid-state diode-pumped, frequency-doubled Nd:vanadate (Nd:YVO₄) laser with continuous-wave output power of 5.5 W at 532 nm. The Mira Seed is a modelocked ultrafast laser oscillator that uses Titanium:sapphire (Ti:Al₂O₃) as a gain medium to produce ultrashort wide-bandwidth pulses. Ultrashort pulses are generated using Kerr Lens Modelocking technique. Mira Seed laser generates 80 fs long pulses at the wavelength of 805 nm with average output power 600 mW and with the repetition rate of 76 MHz. The output pulses are horizontally polarized.

The optical pulse from the laser system is divided into two separate branches by a beam-splitter (see fig. 5.1) . One part goes directly to the THz emitter, GaAs photoswitch TERASED [3]. THz emitter emits linearly polarized pulses that are around 1 ps long and contain frequencies from 0.1 THz to 3 THz. THz pulses are focused by elliptical mirror to a sample fixed on a diaphragm with aperture located in the focal point of the mirror. THz pulse is transmitted through the sample and focused by another elliptical mirror to a sensor behind a pellicle beam splitter. Pellicle beam splitter is transparent for the THz beam and simultaneously it partially reflects the optical sampling beam.

The second part of optical pulse goes through a delay line, then its polarization is changed to vertical by a half-wave plate and a polarizer, and upon a reflection on a pellicle beam splitter it is directed to the sensor as a sampling beam (collinear with the THz beam). The sensor is a ZnTe crystal where the

electro-optic Pockels effect can occur. Electric field of THz pulse dynamically modifies the permittivity tensor of the sensor, so the sensor becomes birefringent and changes the polarization of an optical sampling pulse. The polarization of sampling pulse is then changed by a Soleil-Babinet compensator used as an adjustable quarter-wave plate (this is because we wish to measure a zero difference signal from photodiodes without THz pulse). Using a Wollaston prism as an analyzer (fig. 5.1), the horizontal and the vertical polarizations are spatially separated and detected by two balanced antiparallel slow photodiodes. The difference signal from photodiodes is processed to a lock-in amplifier. By changing the delay of the sampling pulse we can measure the change of the permittivity tensor in time and from this a time dependence of the electric field of the THz pulse can be retrieved; the difference signal of photodiodes is linearly proportional to the electric THz field in ZnTe. The THz part of the experiment, i. e. from the emitter to the sensor, is placed into a vacuum box to avoid water vapor absorption of THz radiation.

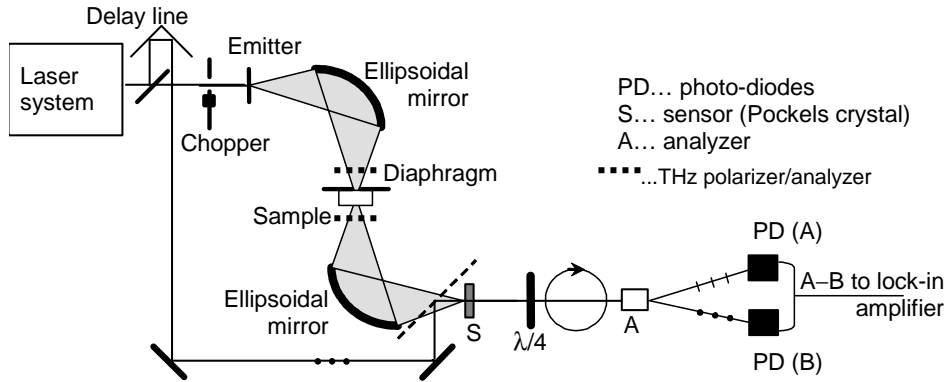


Figure 5.1: Setup of THz steady-state transmission spectroscopy in the time domain.

Total thickness of each sample is measured by mechanical thickness probe with micrometer precision. Then we can easily compute substrate thickness just by subtracting the depth of etching from the total thickness of the sample.

5.2 Data processing

Let us assume that the next experiments are done within the normal incidence. Time-domain THz transmission spectroscopy requires two measurements to be done for each sample: measurement of a THz waveform $\mathcal{E}_{\text{sam}}(t)$ transmitted through the investigated sample and measurement of a reference waveform $\mathcal{E}_{\text{ref}}(t)$ transmitted through a sample with known properties or through a free

space. The complex transmittance $t(f)$ is then calculated as the ratio of Fourier transformations of these waveforms:

$$t(f) = \frac{\mathcal{E}_{\text{sam}}(f)}{\mathcal{E}_{\text{ref}}(f)}. \quad (5.1)$$

We assume that a sample (investigated sample, reference) is a planparallel slab of a homogeneous material. A part of THz beam passes directly through the sample, another part exits the sample after a series of internal reflections (see Fig. 5.2(a) and (b)). For thick samples these reflections appear as echoes well separated in time. The total transmittance of the sample can be expressed as a sum of all contributions [9]:

$$t(f) = \sum_{k=0}^{\infty} t_k(f) = t_1 t_2 \cdot \frac{e^{2\pi i f d n / c}}{1 - (r_1 r_2 \cdot e^{2\pi i f d n / c})^2} \quad (5.2)$$

where the individual contributions read

$$t_k(f) = t_1 t_2 \cdot e^{2\pi i f d n / c} (r_1 r_2 \cdot e^{2\pi i f d n / c})^{2k}, \quad (5.3)$$

where d is the thickness of the sample, n is its refractive index, c is the velocity of light in vacuum, t_1 , t_2 are the amplitude transmittances of the input and output interface and r_1 , r_2 are internal amplitude reflectances for the input and output interface, respectively. In the case of a homogeneous sample (also the reference) we obtain:

$$t_1 = \frac{2}{n + 1} \quad (5.4a)$$

$$t_2 = \frac{2n}{n + 1} \quad (5.4b)$$

$$r_1 = r_2 = \frac{n - 1}{n + 1} \quad (5.4c)$$

Our samples consist typically of a substrate and of an etched layer. The optical thickness of the etched layer is quite small, such that all the echoes originating from multiple reflections inside the layer overlap in time. In contrast, the substrate is optically thick and the individual echoes are resolved in time. Equations (5.2) and (5.3) may be used for the retrieval of the refractive index of etched layers, provided t_1 and r_1 are appropriately defined as the transmission through air/etched-layer/substrate interface:

$$t_1 = \left[\frac{4n_{s,p}}{(n_{s,p} + 1)(n_{s,p} + n)} \right] \left[\frac{e^{2\pi i f n_{s,p} d_{\text{el}} / c}}{1 - \left(\frac{n_{s,p} - 1}{n_{s,p} + 1} \right) \left(\frac{n_{s,p} - n}{n_{s,p} + n} \right) e^{4\pi i f n_{s,p} d_{\text{el}} / c}} \right] \quad (5.5a)$$

and internal reflection on an etched layer

$$r_1 = \frac{\left(\frac{n_{s,p}-1}{n_{s,p}+1}\right) e^{4\pi i f n_{s,p} d_{el}/c} - \frac{n_{s,p}-n}{n_{s,p}+n}}{1 - \left(\frac{n_{s,p}-1}{n_{s,p}+1}\right) \left(\frac{n_{s,p}-n}{n_{s,p}+n}\right) e^{4\pi i f n_{s,p} d_{el}/c}} \quad (5.5b)$$

where d_{el} is the thickness of etched layer (depth of etching), $n_{s,p}$ is the effective refractive index of the etched layer for s or p polarization and n is the refractive index of the substrate.

In order to improve the spectral resolution long time-scans are needed (see example in Fig. 5.2). In these scans we distinguish echoes (internal reflections) coming from the emitter and sensor. To remove these artifacts we need to measure a long time-scans of a reference and then process the signal from the sample using deconvolution (see Fig. 5.2(b) and (c)). Using the clear signal (i. e. without these echoes) of the sample and reference we can determine refractive index of the etched-layer by using numerical solution of equations (5.2) or (5.3) with (5.5a) and (5.5b) where $t(f)$ is obtained from the experiment.

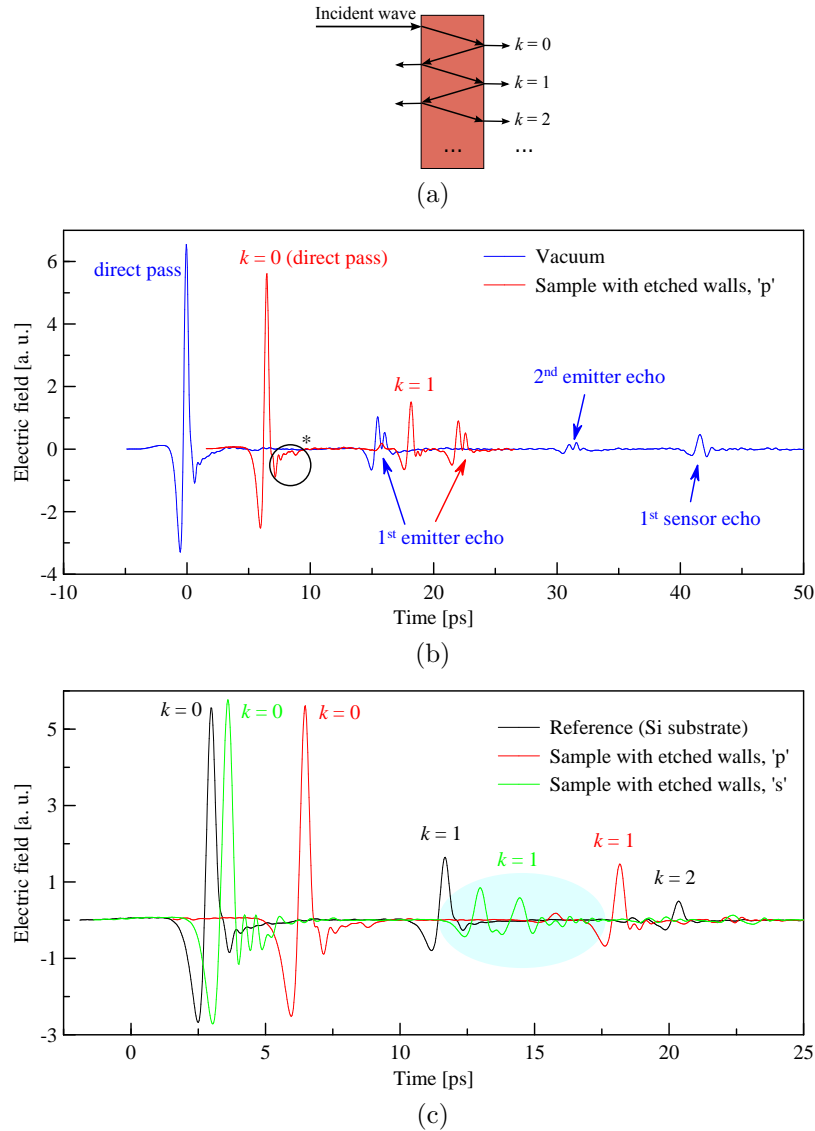


Figure 5.2: (a) Illustration of internal reflections in the sample. The directly passing wave has index $k = 0$. (b) Example of measured waveforms in the presence and absence of a thick sample with etched walls (red and blue lines, respectively). In this case, internal reflections and echoes are clearly separated in time. * We can see a modulation due to the multiple reflections inside the etched layer (following (5.5a)). (c) Example of measured deconvoluted waveforms of reference and sample. Emitter echo is removed. The highlighted part shows the internal echo of the sample for 's' polarization; since the etched layer is deep, the echo consists of partially separated peaks.

5.3 Anisotropy of an etched layer

What is the anisotropy of a sample composed of walls? Can it be described by a permittivity tensor and by an indicatrix? This was the first problem I solved within my master work as an introduction to the optical properties of our samples.

Theoretical approach:

- According to section 4.1, for angle of incidence $\theta = 0^\circ$ (see Fig. 5.3) the effective permittivity of etched walls reads (equations (4.2a), (4.2b)):

$$\epsilon_s = \frac{\epsilon_{\text{Si}}}{\epsilon_{\text{Si}} - x(\epsilon_{\text{Si}} - 1)} = n_s^2 \quad (5.6a)$$

$$\epsilon_p = 1 + x(\epsilon_{\text{Si}} - 1) = n_p^2 \quad (5.6b)$$

- For angle of incidence $\theta = 90^\circ$ (propagation perpendicular to the walls, through a layered medium with a subwavelength period) condition $nk_0d \ll 1$ is satisfied and transfer matrices (4.6) of Si and air layers can be approximated by

$$S_{\text{Si}} \approx \begin{bmatrix} 1 & ik_0dx \\ i\epsilon_{\text{Si}}k_0dx & 1 \end{bmatrix}, \quad (5.7)$$

$$S_{\text{air}} \approx \begin{bmatrix} 1 & ik_0d(1-x) \\ ik_0d(1-x) & 1 \end{bmatrix}, \quad (5.8)$$

where x is the filling factor. The bilayer is described by

$$S = S_{\text{Si}}S_{\text{air}} \approx \begin{bmatrix} 1 & ik_0d \\ ik_0d((1-x) + \epsilon_{\text{Si}}x) & 1 \end{bmatrix}, \quad (5.9)$$

which means that the effective permittivity for this geometry reads

$$\epsilon_{\text{eff}} = (1-x) + \epsilon_{\text{Si}}x \equiv \epsilon_p. \quad (5.10)$$

From the theoretical point of view our metamaterial should behave like a negative uniaxial crystal with effective permittivity tensor

$$\hat{\epsilon}_{\text{eff}} = \begin{bmatrix} \epsilon_s & 0 & 0 \\ 0 & \epsilon_p & 0 \\ 0 & 0 & \epsilon_p \end{bmatrix}. \quad (5.11)$$

Thus n_s corresponds to extraordinary refractive index, which depends on the incident angle of the beam, and n_p corresponds to ordinary refractive index,

which does not depend on the incident angle of the beam. As a result, the dependence of n_s on (outer) incident angle θ reads

$$n_s^2(\theta) = n_s^2 + \sin^2(\theta) \left(1 - \frac{n_s^2}{n_p^2} \right), \quad (5.12)$$

where n_s denotes the refractive index of the wave with a polarization perpendicular to etched walls for normal incidence, i. e. for $\theta = 0^\circ$.

For the experimental verification of this hypothesis we used one of the samples studied previously in [49], thus we knew all necessary parameters (see fig. 5.3):

$d_{\text{el}} = 80 \mu\text{m}$ (depth of etching),

$d_{\text{sub}} = 310 \mu\text{m}$ (substrate thickness),

$w = 6 \mu\text{m}$ (width of walls),

$s = 6 \mu\text{m}$ (width of lines),

and thus the corresponding filling factor is $x = 0.5$. Using equations (5.6a) and (5.6b) we could calculate the expected refractive indices for normal incidence:

$n_s = 1.36$ and $n_p = 2.52$.

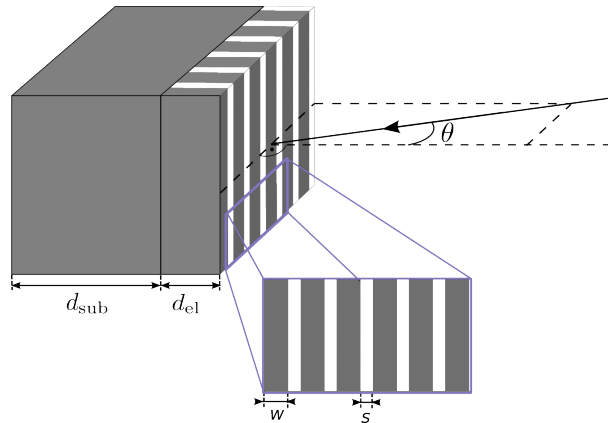
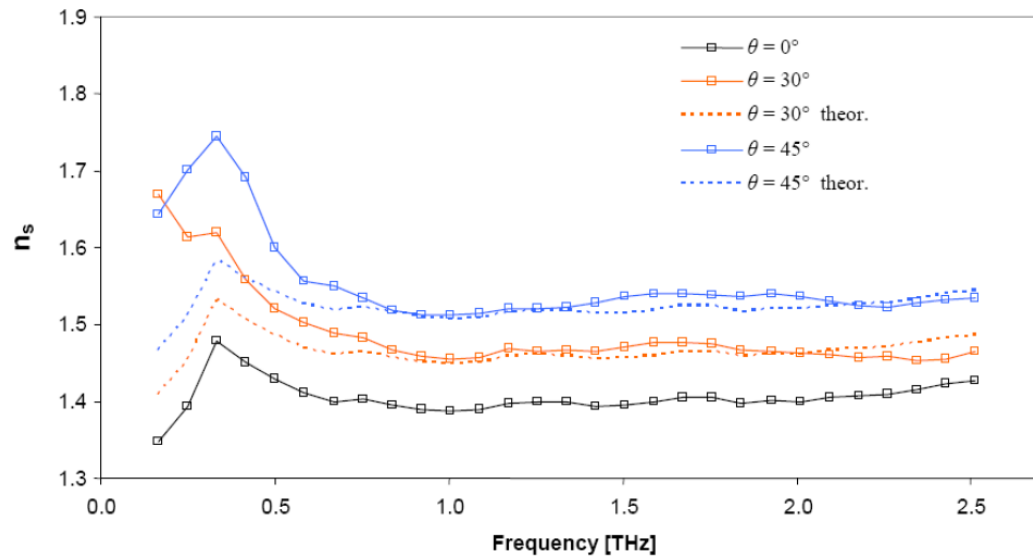


Figure 5.3: Scheme of a measured sample.

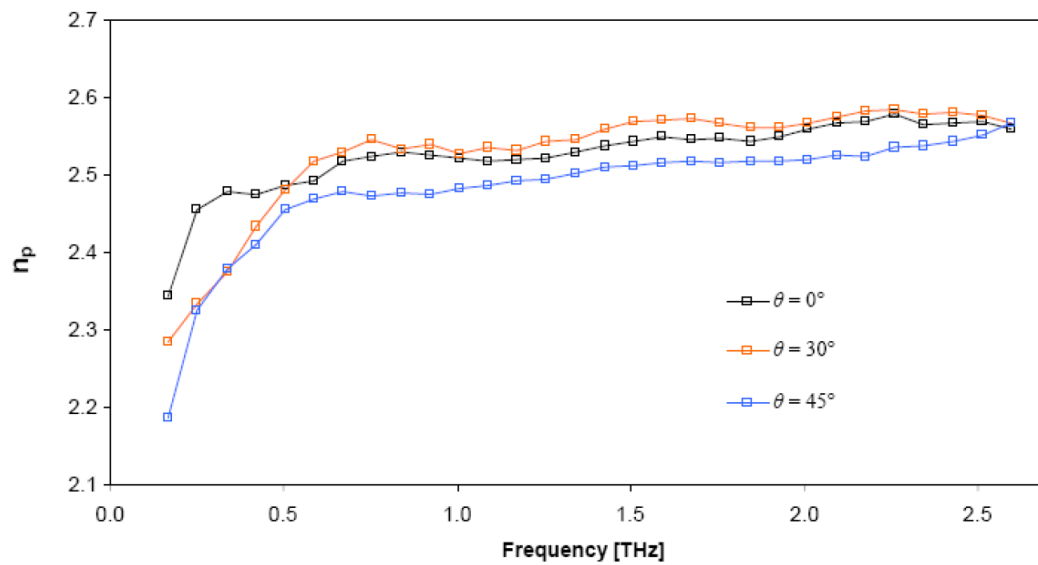
To fix the sample in the focal point of elliptical mirror (see fig. 5.1) we used diaphragm with aperture of 6 mm, glued sample on it and put it into a holder located in the focal point. We have made measurements for incidence angles $\theta = 0^\circ, 30^\circ, 45^\circ$. THz beam was linearly polarized in horizontal direction, thus each measurement was done twice: one with horizontally oriented etched walls ('p' polarization) and the other one with vertically oriented etched walls ('s' polarization). The results of measurements are shown in fig. 5.4. Theoretical values of $n_s(\theta)$ were computed using eq. (5.12). We chose to compute this data from measured values of n_s and n_p for normal incidence rather than from values computed from filling factor since the former gives a better picture of

the frequency dependence. The theoretical values fits well the experimental values.

From graphs in Fig. 5.4 we see that refractive index increases (decreases) for 's' ('p') polarization at lower frequencies; these frequencies are diffracted by a diaphragm because the wavelength is comparable to the diameter of the diaphragm. Since we assume that metamaterial layer behaves as a negative uniaxial crystal ($n_s < n_p$) n_s will increase, however n_p will decrease for lower frequencies. We must emphasize that the results at lowest frequencies are measured with a high error and therefore do not go against the theory. The measurement is affected by a systematic error in the positioning of the sample in the focal point; we estimate the error of the incident angle $\Delta\theta \approx 1^\circ$.



(a)



(b)

Figure 5.4: Dependence of refractive index of etched layer on incident angle; (a) 's' polarization, (b) 'p' polarization

5.4 Samples

Samples were prepared using reactive ion etching (RIE) by our collaborators at University of Lille, Lille, France. Our thanks go to Karine Blary who prepared all the samples for my experiments.

A sample looks like a plate (wafer) of 9 mm x 9 mm with an approximately-centered etched square area of 7 mm x 7 mm. The first step was an experimental characterization of effective properties of the samples. We need to know the refractive indices of each layer for 's' and 'p' polarization, the depth of etching and the thickness of the substrate. We selected four samples for each type of structure and measured them. Samples 1 and 2 were used as obtained, samples 3 and 4 were rinsed in acetone for two hours prior to the measurement in order to remove possible traces of resist from inside the structure. We did not find any significant difference between these two kinds of samples. For THz time domain measurements we centered samples on a diaphragm with an aperture of 5 mm to the focal point of THz radiation as shown in Fig. 5.1. All samples were measured in transmission under normal incidence. The total thickness d (i. e. sum of thicknesses of etched and unetched part) of each sample is in table 5.1. Absolute error of thickness measurement is estimated to $1 \mu\text{m}$ and reflects mainly systematic errors (dust, planparallelity of etched layer).

d [μm]	1	2	3	4
Walls 20 μm	459.6	454.6	458.1	455.4
Walls 48 μm ($a = 28 \mu\text{m}$)	455.0	453.5	441.1	452.8
Walls 48 μm ($a = 30 \mu\text{m}$)	439.4	450.1	444.6	439.8
Walls 119 μm ($a = 28 \mu\text{m}$)	529.7	530.7	529.4	529.8
Walls 119 μm ($a = 30 \mu\text{m}$)	533.1	531.2	530.4	530.1
Pillars 40.5 μm	463.1	459.6	464.1	458.4
Pillars 81 μm	449.5	447.3	448.8	449.2

Table 5.1: Total thickness of measured samples.

5.4.1 Walls 20 microns

The layer B is composed of periodic etched walls that are $d_b = 20 \mu\text{m}$ deep and $16 \mu\text{m}$ wide (space between two walls is $4 \mu\text{m}$ wide). The measured refractive indices are in figure 5.11.

All measured samples have similar value of the refractive index which is close to the theoretical value. Mismatch is caused mainly by two reasons: error

in total thickness of sample (which is critical when evaluating refractive index from measured spectrum) and mismatch in the filling factor. The former was discussed previously and corresponds to a systematic error of $1 \mu\text{m}$; the latter can be deduced from SEM images, see fig. 5.5. The period of etching was decreased from $16 \mu\text{m}$ to $15 \mu\text{m}$ to compensate for an expected increase of the refractive index at higher frequencies. After the experiments we observe that this was not necessary and as a result we obtain both refractive indices slightly below their theoretical values. However, the layer B is only $20 \mu\text{m}$ thick, so this will not cause large errors in wave plates.

5.4.2 Walls 48 microns

This type of sample is made twice: with period $a = 28 \mu\text{m}$ and with period $a = 30 \mu\text{m}$. The measured refractive indices are in fig. 5.12 ($a = 28 \mu\text{m}$) and fig. 5.13 ($a = 30 \mu\text{m}$).

Refractive index n_p is rather constant, but we can see the expected increase of n_s for frequencies above 1.5 THz. Samples with period $a = 30 \mu\text{m}$ are closer to theoretical values than those with period $a = 28 \mu\text{m}$. We suppose that this is a result of a small underetching, i. e. etched lines between walls are wider than planned. This is found for both types of samples, but for the larger period we obtain a smaller mismatch.

Samples 3 and 4 in 5.13 have lower refractive indices than samples 1 and 2. We suppose that this is because some resist have been removed by acetone, or because of different etching. In fact, all samples (of one type) are etched in a single flat silicon wafer at the same time and etching in the middle can differ from etching on the edges.

Regardless the photo on fig. 5.6 shows a testing sample with a different period of etching we assume that our samples are made in a same qualitative manner.

5.4.3 Walls 119 microns

Same as walls 48 microns, this type of sample is made twice: with period $a = 28 \mu\text{m}$ and with period $a = 30 \mu\text{m}$. The measured refractive indices are in fig. 5.14 ($a = 28 \mu\text{m}$) and fig. 5.15 ($a = 30 \mu\text{m}$).

The characteristics of these samples are similar to those with 48 microns walls. Refractive indices are lower due to strong underetching which can be seen from the photos of testing samples (Fig. 5.7 and Fig. 5.8). The first photo (Fig. 5.7) is a sample with proposed depth and filling factor but different period. The sample in the second photo (Fig.5.8) was etched with a higher period and clearly the underetching is tempered however not completely eliminated.

The lower values of the indices than planned in this type of sample are not as tolerable as in the case of 20 μm walls because these walls are much deeper and a little mismatch in refractive indices causes much different phase retardation. On the other hand, one can see that the difference between theoretical and measured values is almost the same for both polarizations and since phase retardation is defined by a relative difference of these indices (birefringence), a wave plate that uses this type of samples should give good phase shift near central frequency.

5.4.4 Pillars 40.5 microns

Samples with etched pillars serve as antireflective layers for air/silicon interface. Especially, samples with pillars depth of 40.5 μm are used for $f_0 = 1$ THz. The measured refractive indices are in figure 5.16.

Since pillars are isotropic we use '1' and '2' notation instead of 's' and 'p', however, polarizations '1' and '2' remain orthogonal. We expect the same value of refractive index for both polarizations (and thus for any polarization). Graphs in Fig. 5.16 show that between 0.3-1.7 THz the refractive indices are in a good agreement with theoretical values.

Photo of testing sample in Fig. 5.9 shows that there is a little relict of silicon between the pillars but we do not expect that this should break our next experiments.

5.4.5 Pillars 81 microns

These samples are designed to be an antireflective layers for air/silicon interface for $f_0 = 0.5$ THz and shows similar characteristics as the pillars with depth of etching 40.5 μm . The measured refractive indices are in figure 5.17.

The photo of testing sample on Fig. 5.10 shows that there is a little under-etching under the mask, but since refractive indices are in a good agreement with its theoretical values and the depth of etching is quite precisely 81 μm we suppose that these samples will work as expected.

5.4.6 Summary

For all samples there is a higher noise in measurement at the lower frequencies due to the diffraction on the input aperture (holder). This is because the corresponding wavelength is comparable to the diameter of the diaphragm. The diffraction losses prove the non-zero extinction coefficient. In the range of 0.5-2 THz the extinction coefficients for both polarizations vanish, thus there are no losses due to absorption or scattering on an etched structure or a substrate. For

the frequencies higher than 1.5 THz and high period of etching the increase of the refractive indices occurs as predicted in the section 4.3.2.

From the graphs showing the results we can see that the lower the depth of etching is, the higher the dispersion of refractive index is. On the other hand, a wave plate is more sensitive to changes in the samples with high depths of etching. Therefore we can say that all etched layers plays similar role in a wave plate.

To see the differences between the measured parameters of the etched layers and their theoretical values we summarize the results in table 5.2. The depths are measured in the SEM photos of testing samples and thus they show an estimate of depths of used samples rather than the precise values. The filling factors were calculated form the average value of the measured THz refractive indices.

f_0 [THz]	C			B		D	
	d_c [μm]	x_{c1}	x_{c2}	d_b [μm]	x_b	d_d [μm]	x_d
0.5	81.6	0.80	0.80	20.7	0.72	124.6	0.75
	(81.0)					(119.0)	(0.85)
1	39.7	(0.82)	(0.82)	(20.0)	(0.75)	46.6	0.83
	(40.5)					(48.0)	(0.85)

Table 5.2: Comparison of experimental and theoretical parameters of the etched layers. Theoretical values are in the brackets.

Although some of the parameters differ from their theoretical values we find the samples quite good and the results provide us with a new knowledge that can be used as a basis for the next work.

5.4.7 SEM photos and graphs

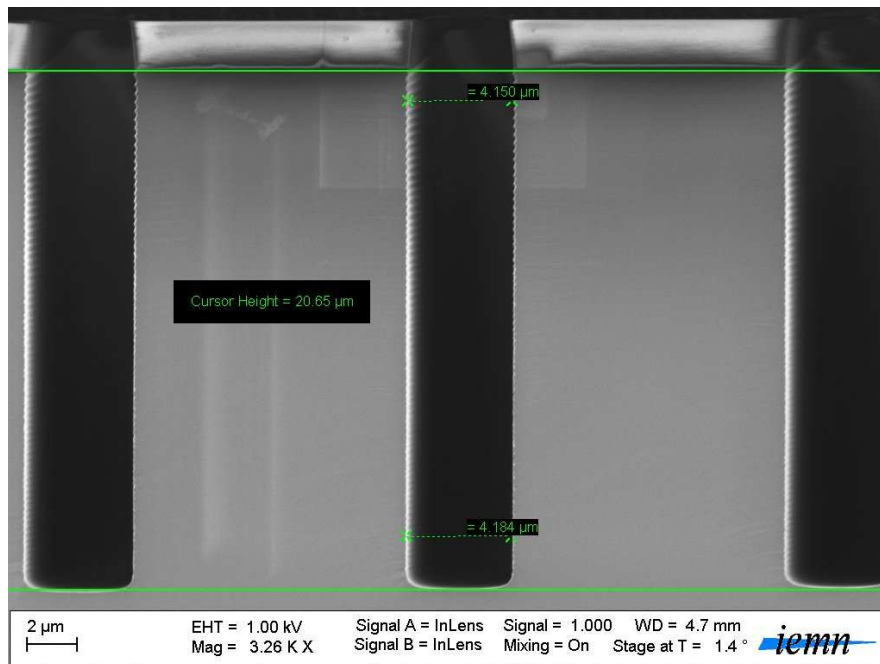


Figure 5.5: SEM photo of testing sample with 20 μm deep etched walls.

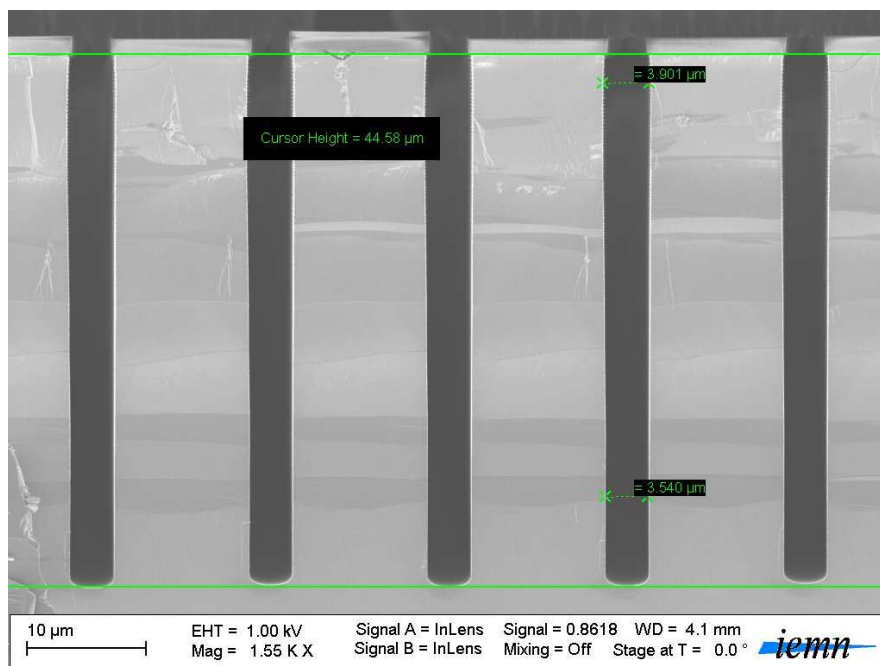


Figure 5.6: SEM photo of testing sample with 48 μm deep etched walls.

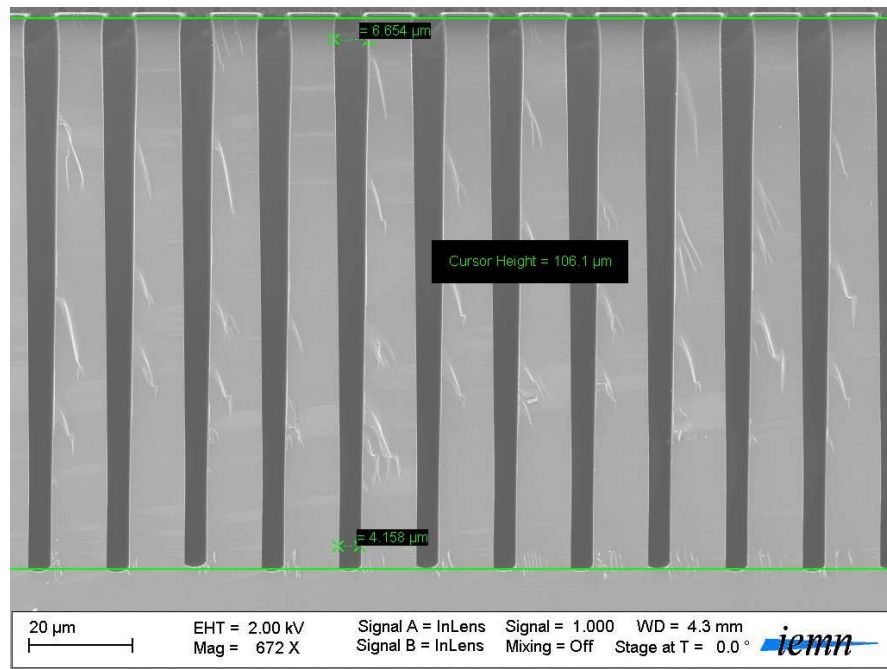


Figure 5.7: SEM photo of testing sample with $119 \mu\text{m}$ deep etched walls and periode $a = 15 \mu\text{m}$.

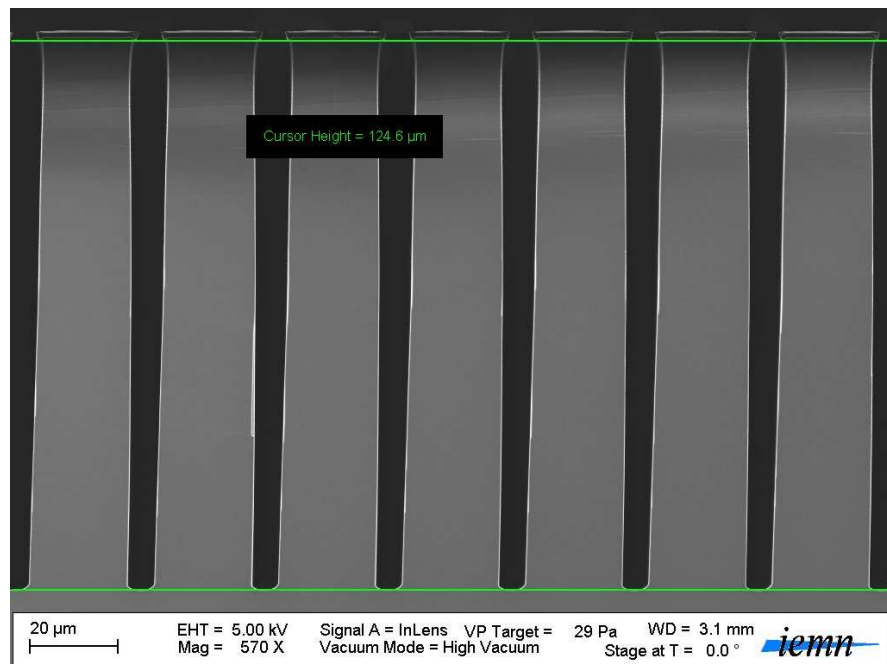


Figure 5.8: SEM photo of testing sample with $119 \mu\text{m}$ deep etched walls and periode $a = 28 \mu\text{m}$.

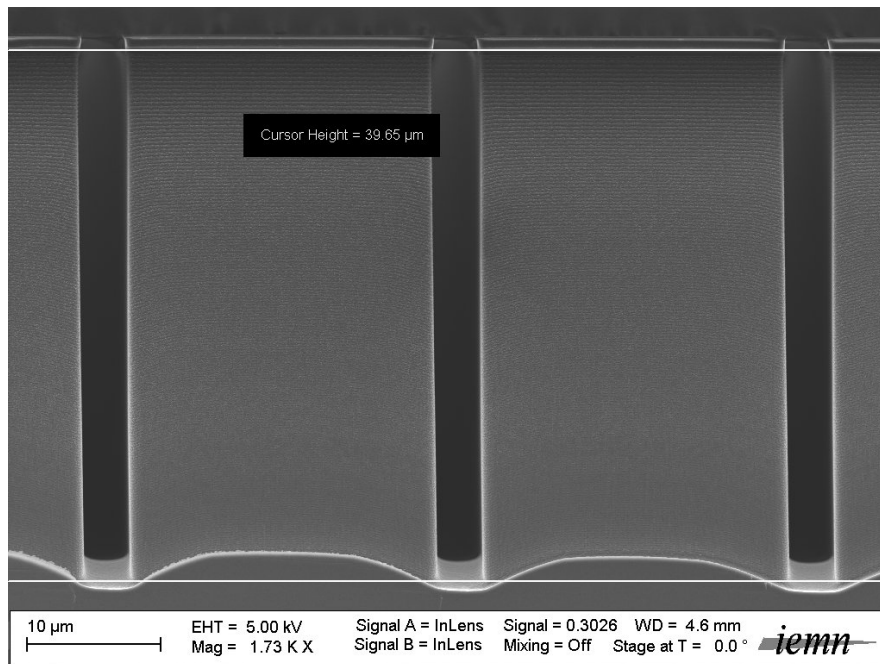


Figure 5.9: SEM photo of testing sample with 40.5 μm deep etched pillars.

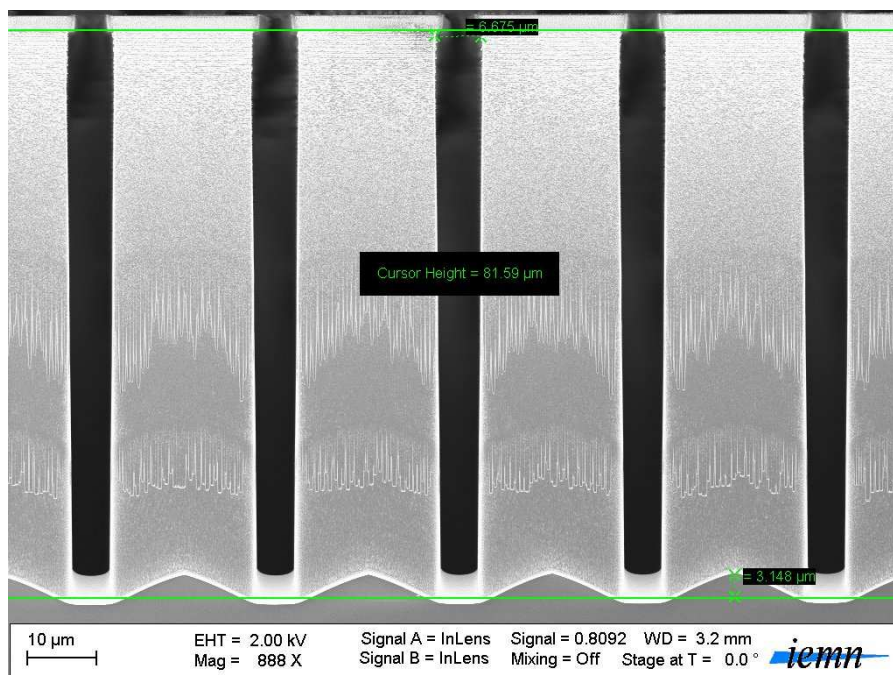


Figure 5.10: SEM photo of testing sample with 81 μm deep etched pillars.

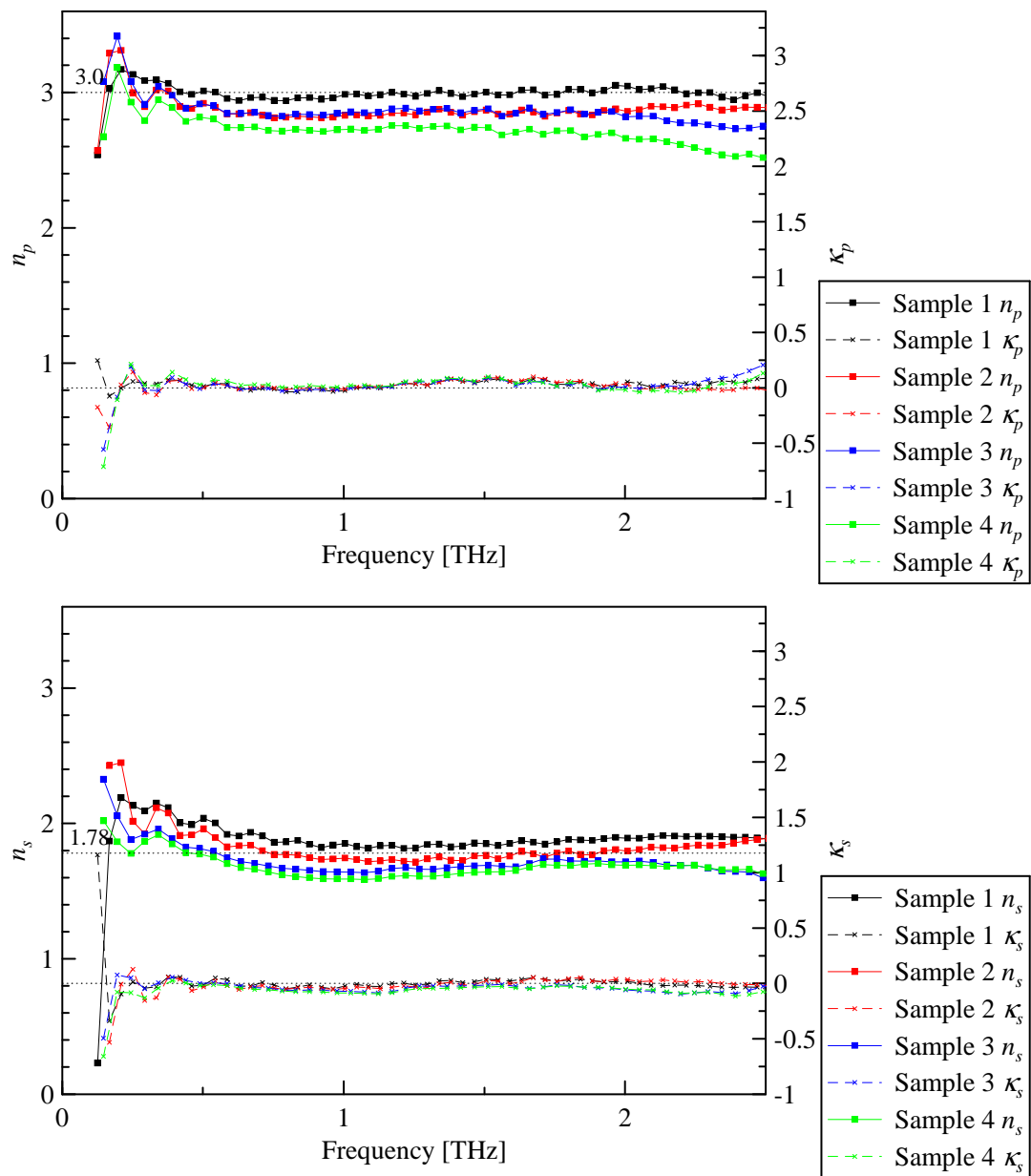


Figure 5.11: Refractive indices n_p , n_s and extinction coefficients κ_p , κ_s of etched walls with depth $20 \mu\text{m}$.

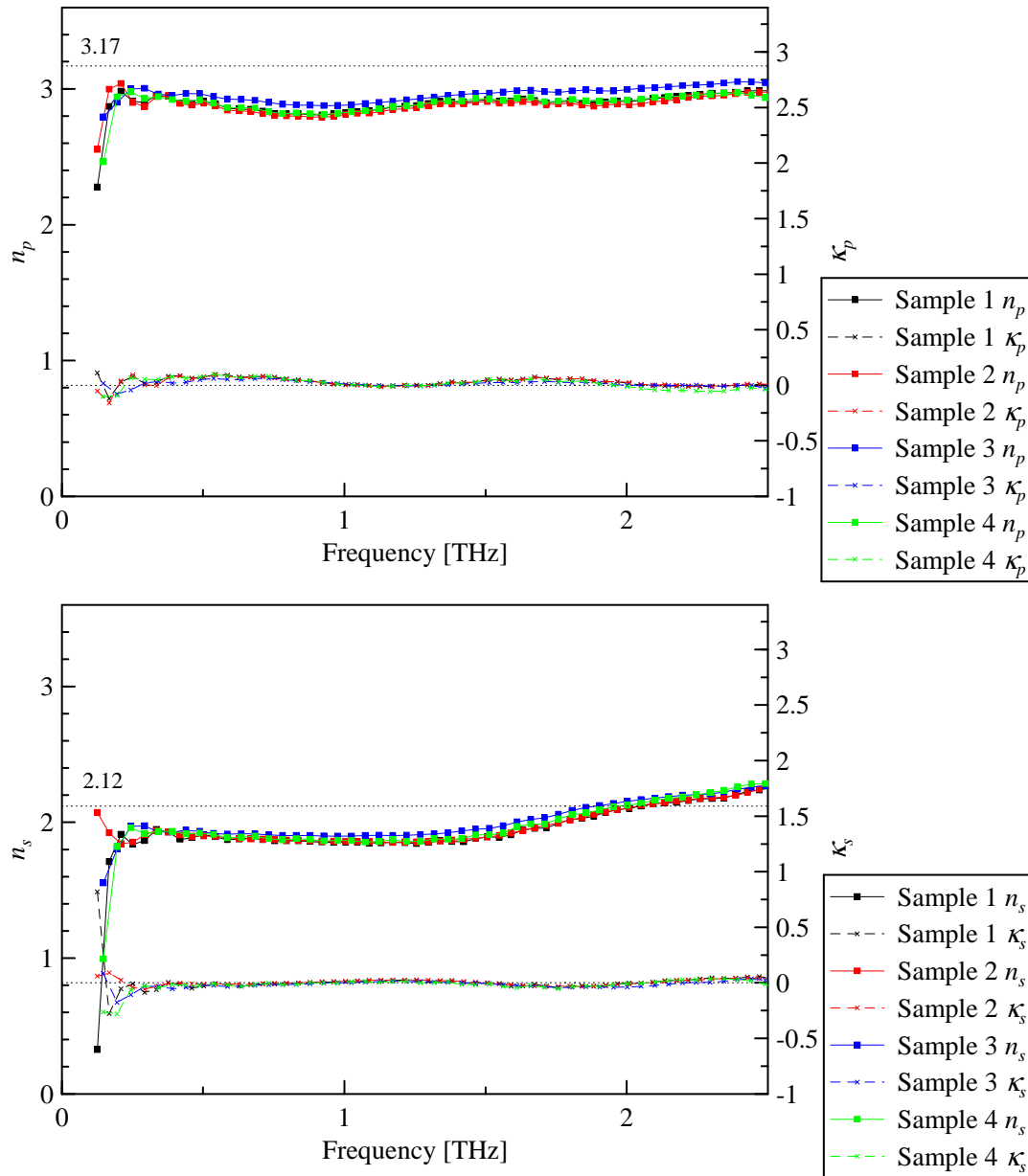


Figure 5.12: Refractive indices n_p , n_s and extinction coefficients κ_p , κ_s of etched walls with depth $48 \mu\text{m}$ and periode $a = 28 \mu\text{m}$.

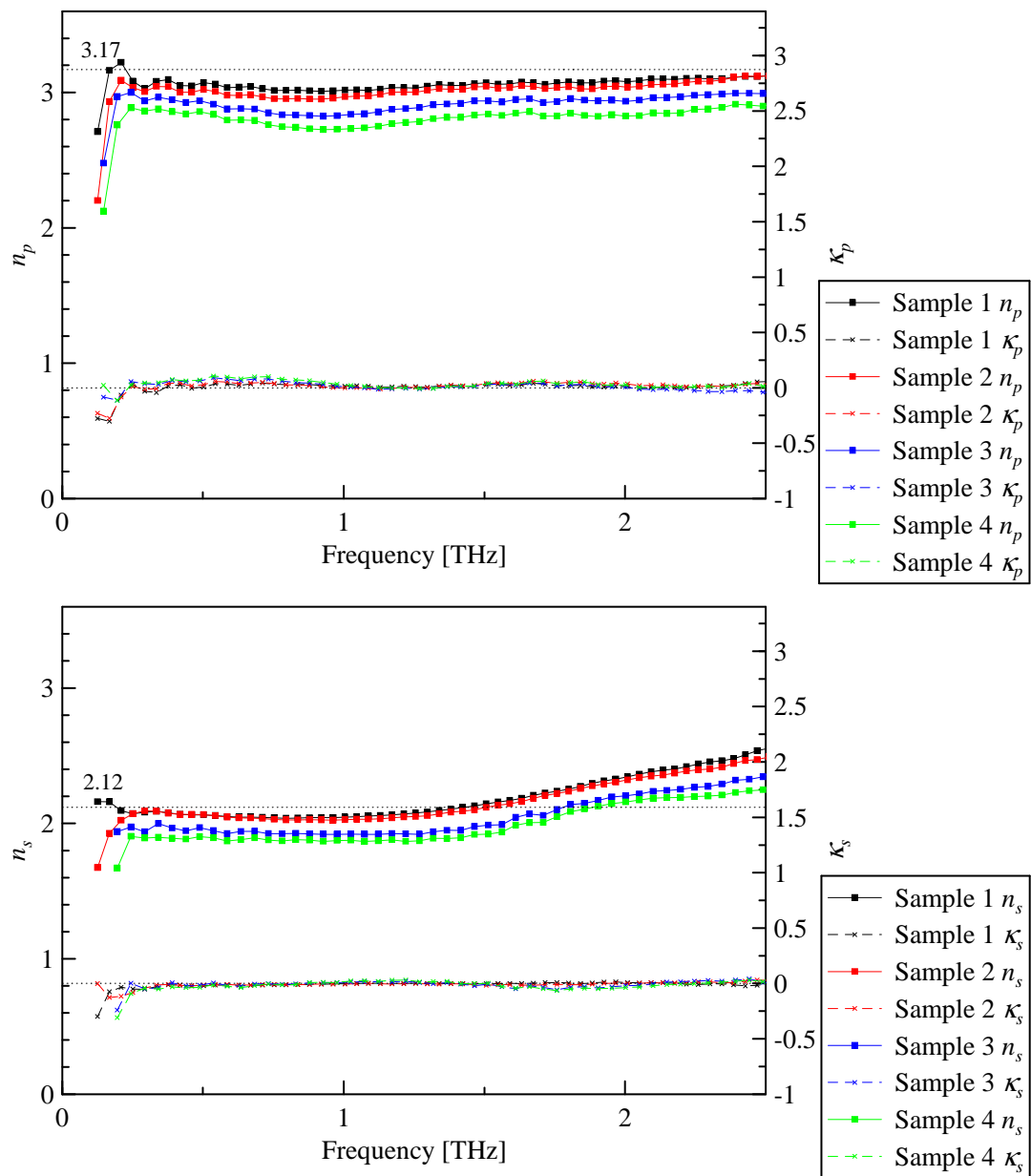


Figure 5.13: Refractive indices n_p , n_s and extinction coefficients κ_p , κ_s of etched walls with depth $48 \mu\text{m}$ and period $a = 30 \mu\text{m}$.

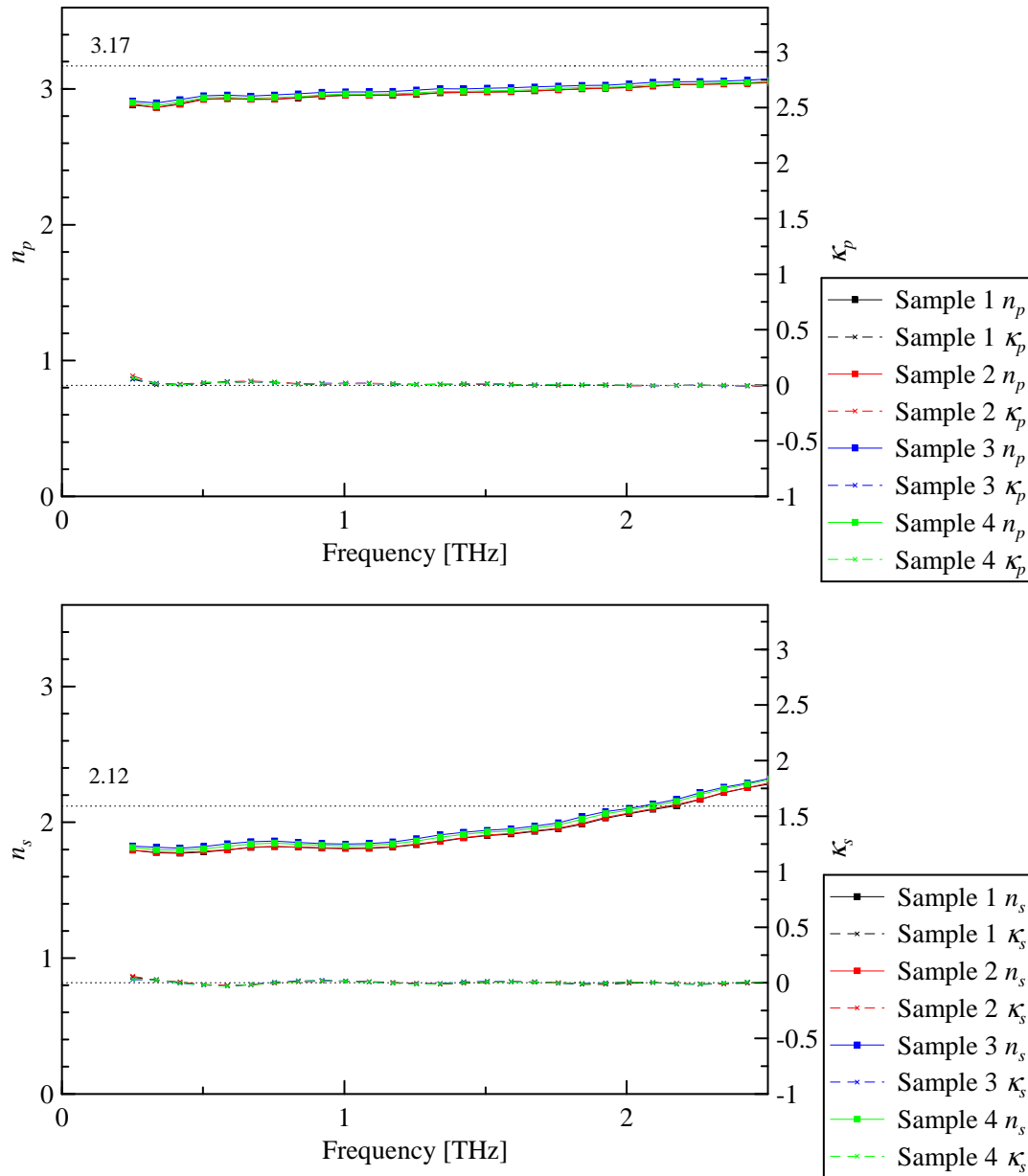


Figure 5.14: Refractive indices n_p , n_s and extinction coefficients κ_p , κ_s of etched walls with depth $119 \mu\text{m}$ and period $a = 28 \mu\text{m}$.

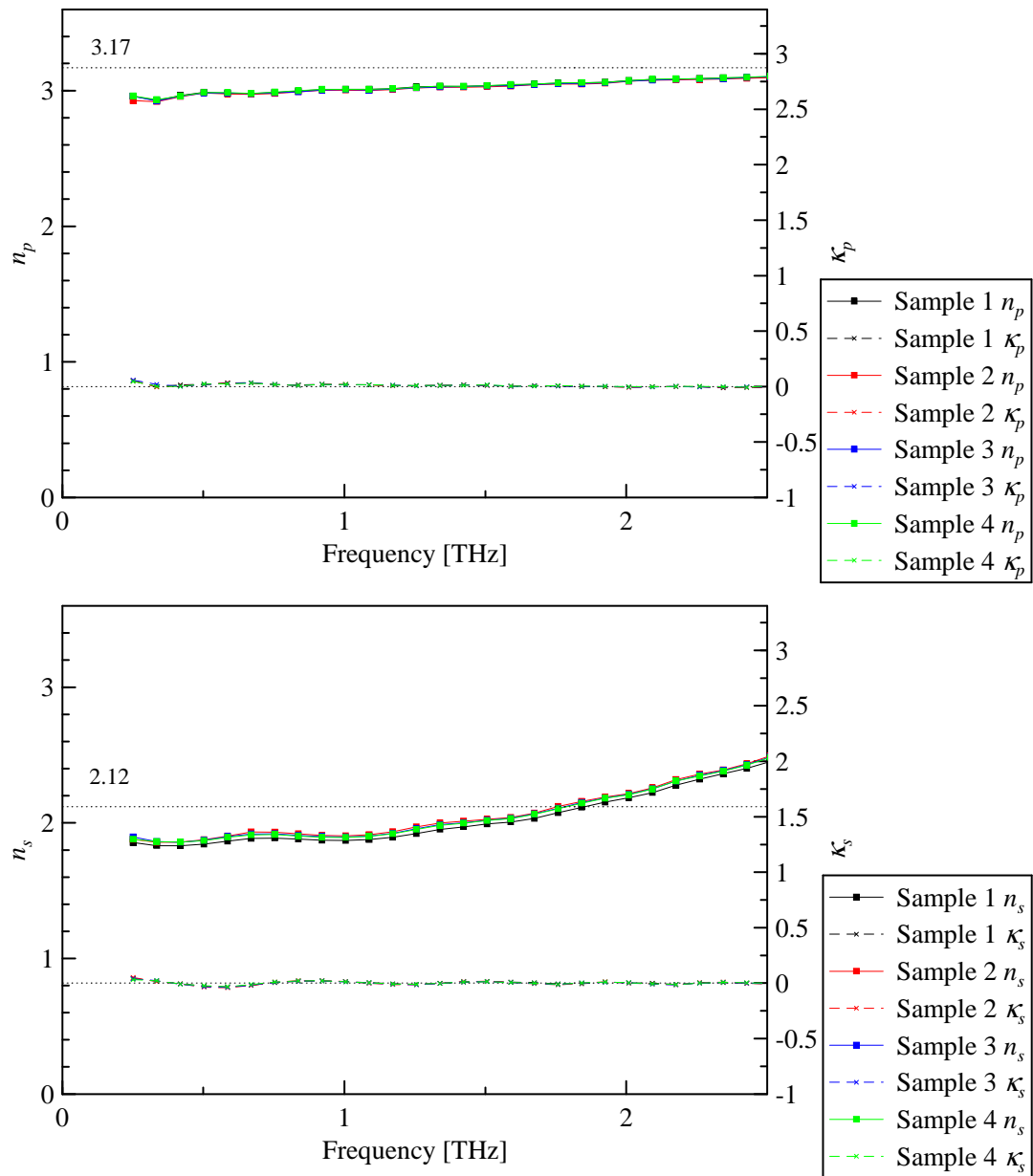


Figure 5.15: Refractive indices n_p , n_s and extinction coefficients κ_p , κ_s of etched walls with depth $119 \mu\text{m}$ and periode $a = 30 \mu\text{m}$.

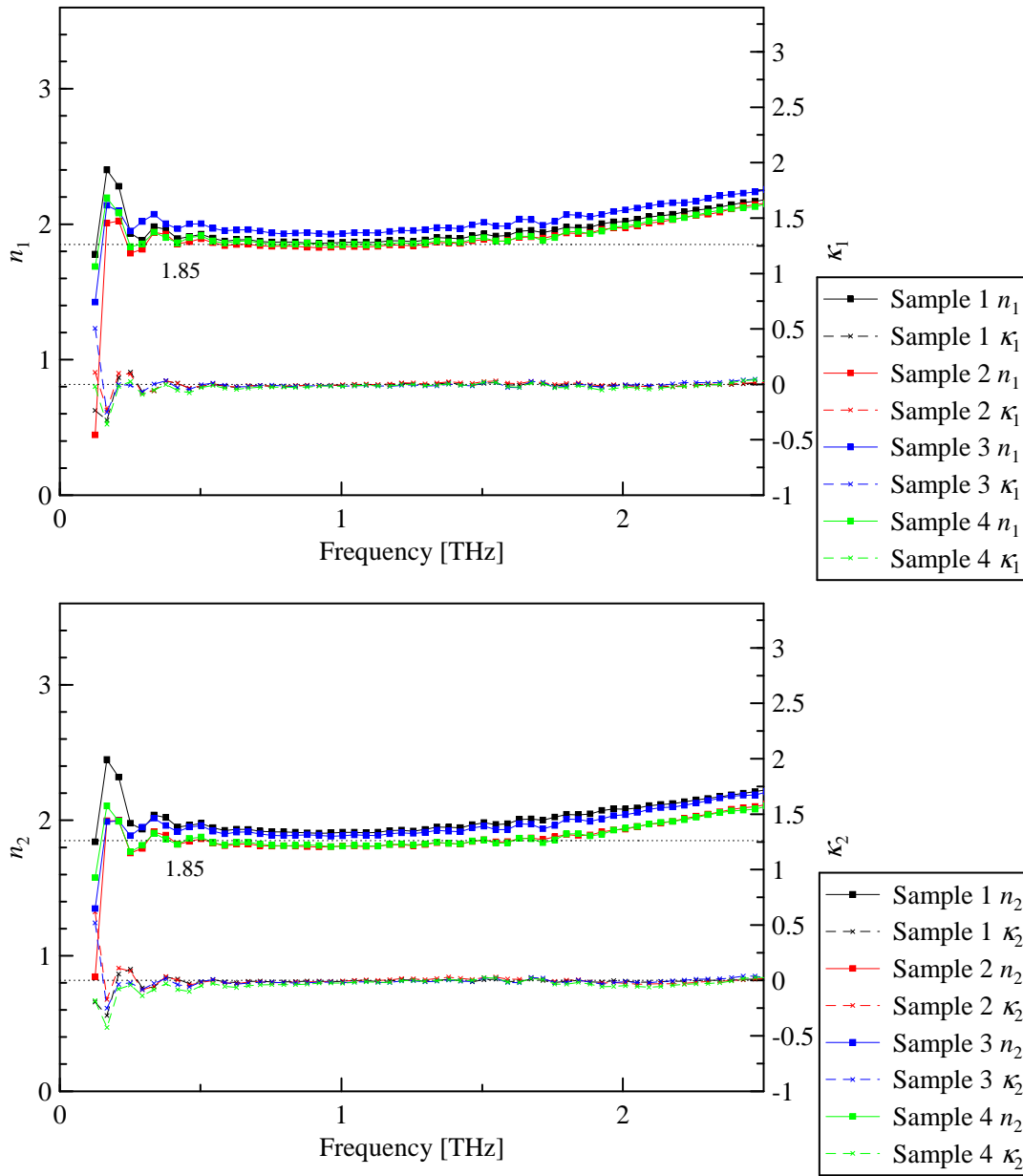


Figure 5.16: Refractive indices n_p , n_s and extinction coefficients κ_p , κ_s of etched pillars with depth $40.5 \mu\text{m}$.

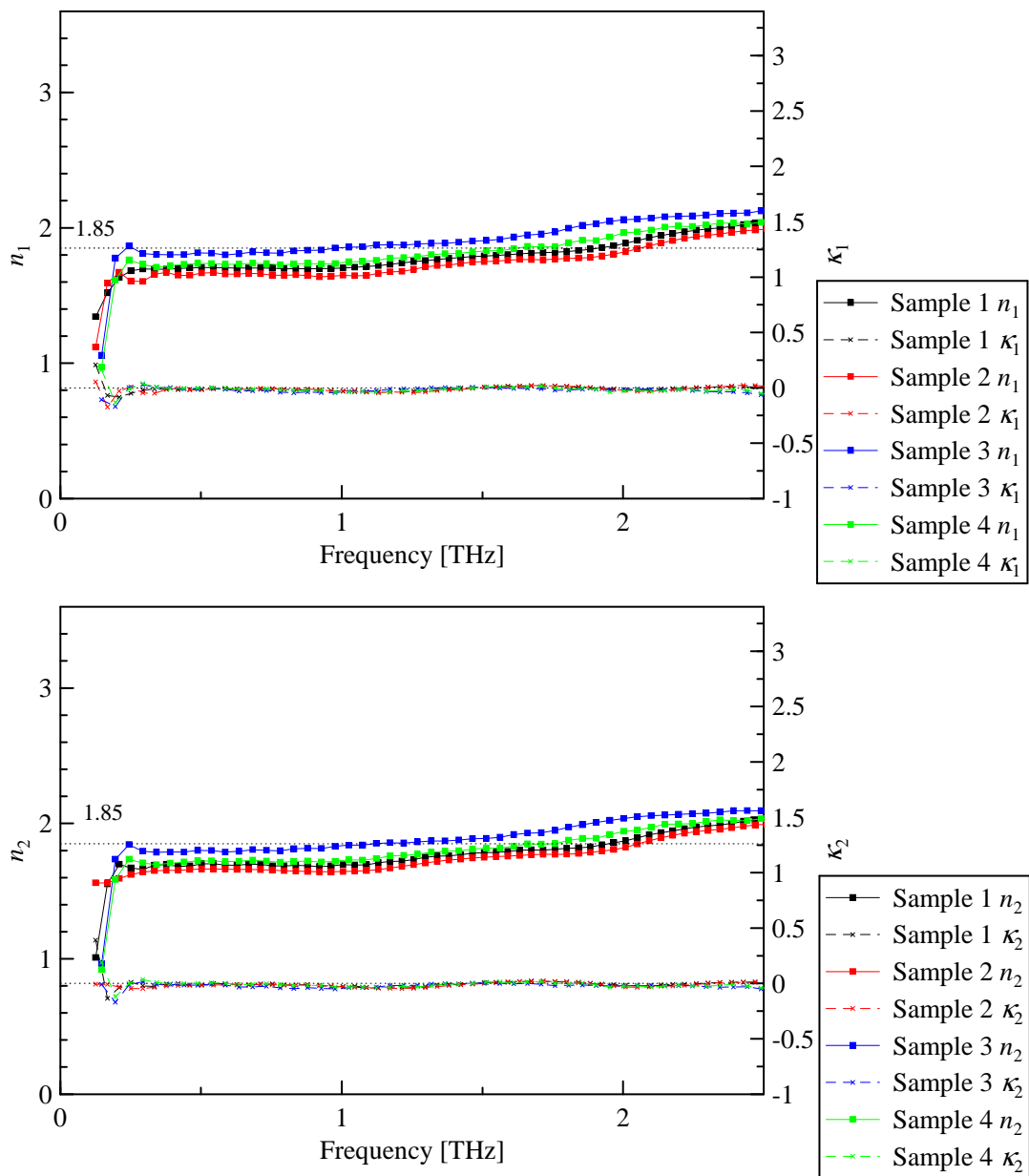


Figure 5.17: Refractive indices n_p , n_s and extinction coefficients κ_p , κ_s of etched pillars with depth $81 \mu\text{m}$.

5.5 Antireflective bilayers

By merging two antireflective layers C (etched pillars) it is possible to prepare an antireflective CC bilayer (see Fig. 5.18) that should transmit central frequency f_0 with amplitude transmission equal to 1. By measuring such a bilayer we can determine whether the layer C works as an antireflective layer between air and Si (substrate). We completed the measurements for both frequencies, i. e. for $f_0 = 0.5$ THz (layer C = pillars $81 \mu\text{m}$) and for $f_0 = 1$ THz (layer C = pillars $40.5 \mu\text{m}$).

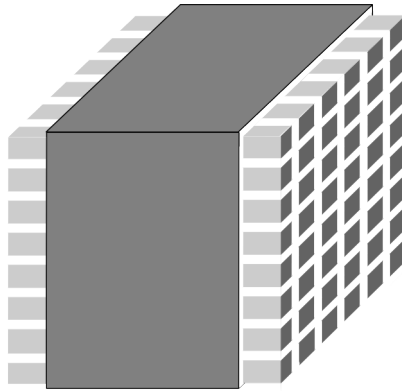


Figure 5.18: Scheme of a CC bilayer.

The amplitude transmission spectra of antireflective bilayers are in Fig. 5.19. We can see that the transmission for f_0 is in each case equal to 100 %. In addition to this the transmission of 1st and 2nd internal echoes of the bilayer is equal to 0 % which demonstrates the antireflective character of the bilayer since the whole intensity on central frequency passes in direct pass. The obvious periodicity of transmittance is given by the periodic condition on thickness of C layer, see Eq. (4.3b). The small modulation of the transmission function is caused due to a Fabry-Perot interference that is more significant in the whole transmission function of the bilayer (including all internal reflections) in Fig. 5.20.

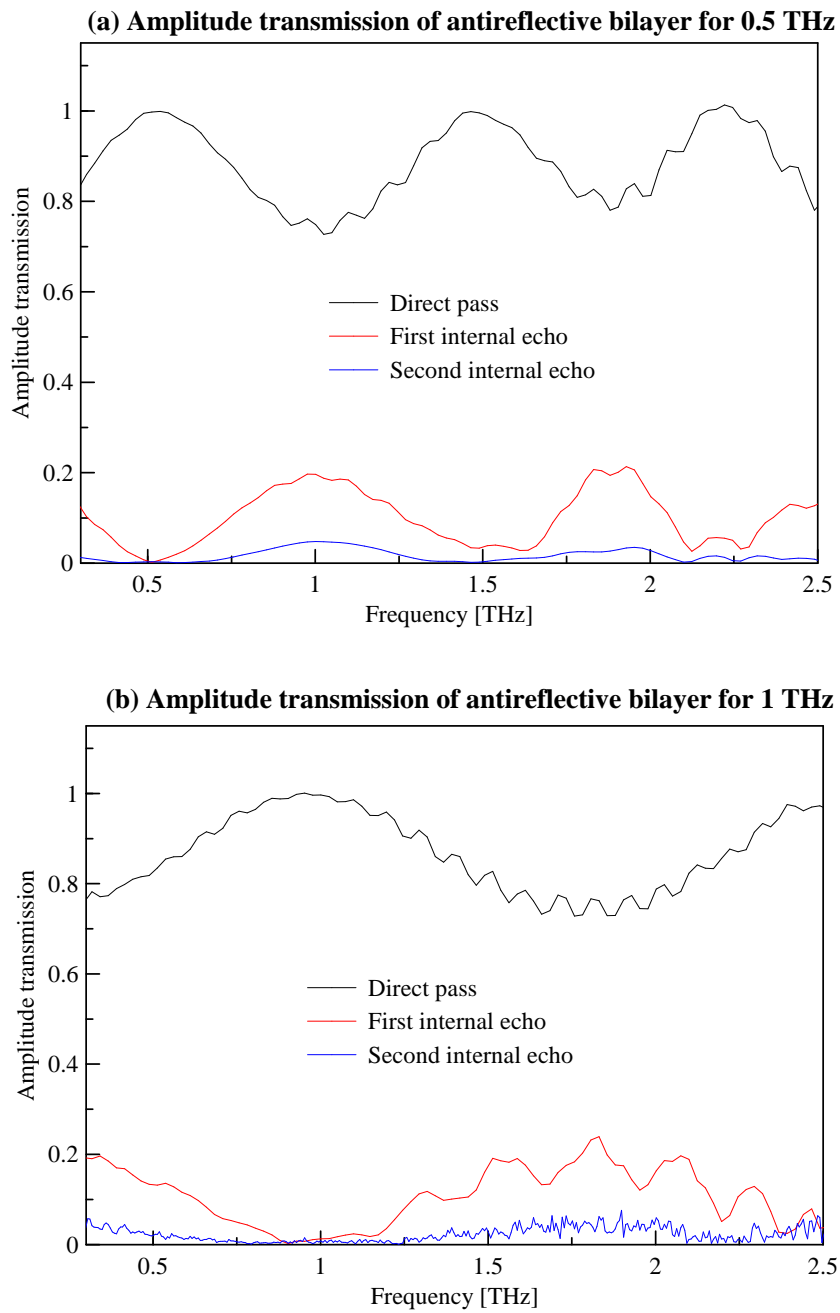


Figure 5.19: Amplitude transmission spectra of direct pass and two internal echoes of antireflective CC bilayers.

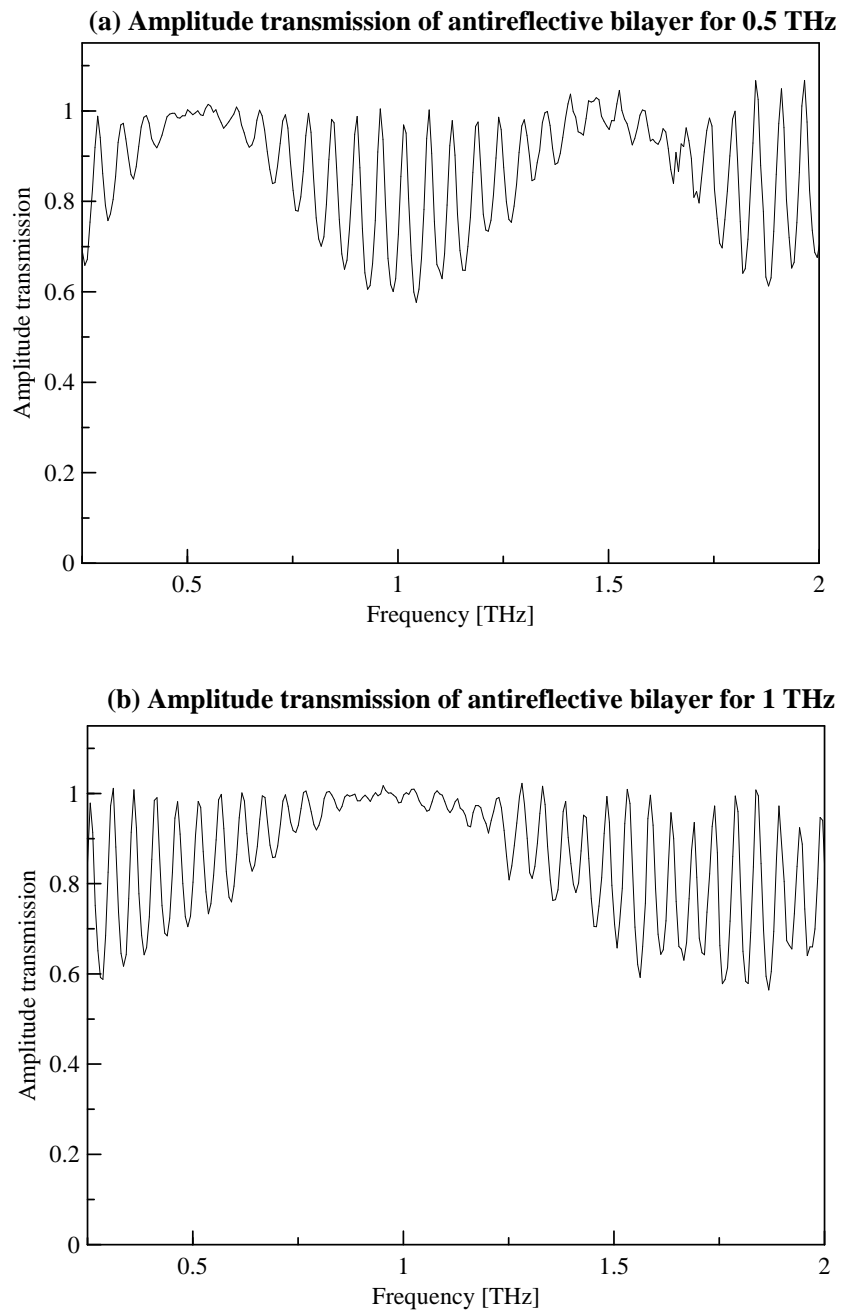


Figure 5.20: Amplitude transmission spectra of antireflective CC bilayers including interference of all internal reflections.

5.6 Wave plates

The samples with etched layers were assembled in an appropriate order and orientation in a holder that consisted of two brass diaphragms with a clear aperture of 5 mm. The samples were not glued together, they were just in a physical contact due to the mechanical screwing of the diaphragms in order to avoid the air layers between samples.

To do this we used a spacer between diaphragms with a thickness equal to the total thickness of a wave plate. Then we recognized that samples are stiff enough to be pressed without any spacer when the diaphragms are screwed using a moderate force. In order to ensure that wave plates are properly assembled and pressed together some preliminary measurements were made before the main experiments.

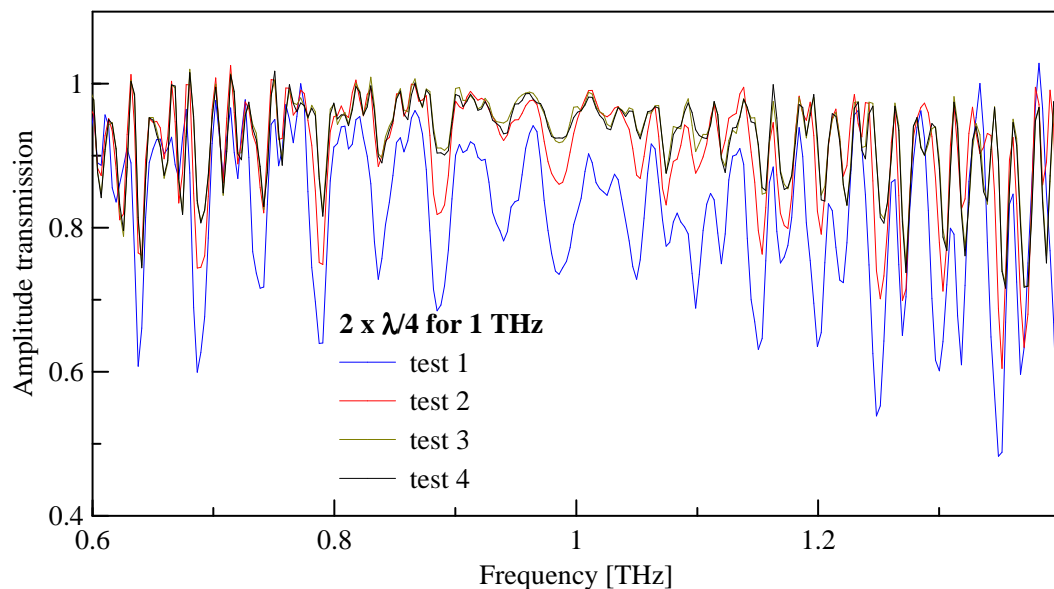


Figure 5.21: The effect of the air spaces between the layers in a wave plate. The screwing force increases with increasing number.

Such test measurements are shown in Fig. 5.21. All four testing experiments were done using a double quarter-wave plate for 1 THz which consisted of 6 pieces (see section 5.6.4). First of all, we screwed the holder slightly and then we used a little more force to screw the diaphragms in each next test until there was no obvious difference in the tests (test 3 and 4). Similar preliminary measurements were performed for each wave plate.

The air layers cause two effects in the THz spectra. Firstly, the internal interference in a wave plate is more complicated and more significant. Secondly, the samples can be in a skewed incidence instead of a normal incidence. Both

of these effects result in a decrease of amplitude transmission and in deeper interference minima in the measured spectral range (see test 1 in comparison with test 4 in Fig. 5.21).

By a complete wave plate characterization we mean knowledge of the absolute values of amplitude transmission for 's' and 'p' polarizations (t_s and t_p , respectively), the relative amplitude transmission (t_p/t_s) and the phase retardation ($\Gamma = \phi_p - \phi_s$). We expect that for central frequency f_0 both t_s and t_p amplitude transmissions of a wave plate are equal to 100%, relative amplitude transmission of a wave plate is equal to 1 and phase retardation is equal to $\pi/2 \approx 1.57$ for a quarter-wave plate, or to $\pi \approx 3.14$ for a half-wave plate. In the next figures we compare theoretical values computed from optimized parameters (theory), theoretical values computed from measured refractive indices of the samples (theory with corrections) and experimental values (experiment). The theoretical data computed from measured refractive indices are expected to fit the experimental data better than the theoretical values computed from optimized parameters. We did not use measured depths of etching for computation since the SEM photographs provide us only with an estimation, instead we used the theoretical values of depths. The parameters used for these calculations are in Tab. 5.3 where d_{el} denotes the thickness of the etched layer and d denotes the thickness of the sample (etched layer + substrate). All samples D have periode $a = 30 \mu\text{m}$.

	Quarter for 0.5 THz				Quarter for 1 THz			
Sample	$d_{el} \mu\text{m}$	$d [\mu\text{m}]$	n_p	n_s	$d_{el} [\mu\text{m}]$	$d [\mu\text{m}]$	n_p	n_s
C: pillars	81	448.8	1.81		40.5	465.0	1.82	
B: walls	20	458.1	2.90	1.80	20	458.1	2.83	1.65
D: walls	119	533.1	2.98	1.87	48	439.4	3.00	2.05
C: pillars	81	449.2	1.73		40.5	458.0	1.82	
	Half for 1 THz				Double quarter for 1 THz			
Sample	$d_{el} \mu\text{m}$	$d [\mu\text{m}]$	n_p	n_s	$d_{el} [\mu\text{m}]$	$d [\mu\text{m}]$	n_p	n_s
C: pillars	40.5	458.4	1.82		40.5	465.0	1.82	
B: walls	20	461	2.80	1.65	20	458.1	2.83	1.65
D: walls	119	530.9	2.93	1.85	48	439.4	3.00	2.05
D: walls					48	450.1	2.98	2.04
B: walls					20	459.6	3.00	1.84
C: pillars	40.5	459.6	1.82		40.5	458.0	1.82	

Table 5.3: Parameters of the samples used for corrections in theoretical calculations.

We prepared two specimens of quarter-wave plates for 0.5 THz and 1 THz and two specimens of half-wave plates for 1 THz. Since there were no significant differences between twins we show only one of them in the plots. We also prepared a double quarter-wave plate for 1 THz that should behave as a half-wave plate for 1 THz.

5.6.1 Quarter-wave plate for 0.5 THz

Complete characterization of a selected quarter-wave plate is in Fig. 5.22. The measured transmission of 'p' polarization fits the optimized theory well; it is only slightly affected by the manufacturing errors.

On the other hand, the measured transmission of 's' polarization is slightly lower than the optimized theoretical results around the central frequency. Moreover there is a local minimum of transmission t_s at $f = 0.5$ THz that amounts 90%. Therefore the relative transmission at central frequency equals to 1.1 instead of 1.

The wave plate is the most sensitive to the properties of the D layer, where high underetching occurred, as seen in section 5.4.3. A small difference in the birefringence leads to a shift of phase retardation as seen in Fig. 5.22. The correct phase shift occurs approximately at $f = 0.43$ THz, where also the relative transmission is close to 1 and its absolute value is above 95 % for both polarizations. We can conclude that this element operates as a quarter-wave plate at $f_0 = 0.43$ THz. The manufacturing errors lead to a shift of the operative frequency instead of breaking the whole functionality. The wave plate can be operated in a relatively narrow spectral range of ± 5 GHz (while the optimized theory shows good results in the range ± 40 GHz).

5.6.2 Quarter-wave plate for 1 THz

Complete characterization of a selected quarter-wave plate is in Fig. 5.23. Transmission for both polarizations are close to the theoretical values and thus a relative transmission is so.

The correct phase retardation is moved approximately by 60 GHz from the central to a higher frequency but we can conclude that this wave plate is in a good match with the optimized theory and the mismatch in the phase retardation is due to a small mismatch in birefringence of B and D layers. We can see that the corrected theory fits the experiments very well and this fact just supports our conclusions.

5.6.3 Half-wave plate for 1 THz

Complete characterization of a selected quarter-wave plate is in Fig. 5.23. This element is very close to the quarter wave plate for 0.5 THz since they differ only in the antireflective C layers.

However we completed this wave plate from a different B and D samples of the same type as one can see from the table 5.3. Thus small differences occur, but the results are the same: transmission of 's' polarization is lower than the optimized theory and as a result the relative transmission and phase retardation does not match the correct values at the central frequency. In this case the relative transmission is close to 1 at approximately 1.1-1.2 THz but the phase retardation is shifted slightly to a lower frequencies than 1 THz like in the case of quarter-wave plate for 0.5 THz. The conclusion is that this element is seriously affected by the manufacturing errors in the samples (D mainly) and does not operate as a designated wave plate at 1 THz nor at frequencies around. At the frequencies around 0.96 THz the phase retardation between the two polarizations is equal to the π . As a consequence the element will turn the polarization plane of a linearly polarized radiation at this frequency. However, the angle of the polarization rotation will slightly differ from 2ϕ (where ϕ is the angle between the input polarization and principal axes or the device).

5.6.4 Double quarter-wave plate for 1 THz

The satisfactory match in the theory and experiments for quarter-wave plate for 1 THz evoked the idea of building the half-wave plate for 1 THz by multiplying the birefringent B and D layers in the quarter-wave plate. In the terminology of the samples the design of this element looks like 'CBDDBC', see the Tab. 5.3 for more details.

Such a structure should exhibit approximately correct phase retardation since the quarter-wave plate does. Indeed it does, as seen in the last graph in fig. 5.25. But on the other hand, the Fabry-Perot interferences for 's' polarization even in optimized theory do not vanish and modulate the transmission. Since the samples are not perfect the modulation for both polarizations occurs. Nevertheless we can see a good match between the corrected theory and experiments. Moreover the relative transmission exhibits a flat plateau around the central frequency.

We can conclude that it is possible to build a half-wave plate by multiplying the birefringent samples in the quarter-wave plate.

5.6.5 Graphs

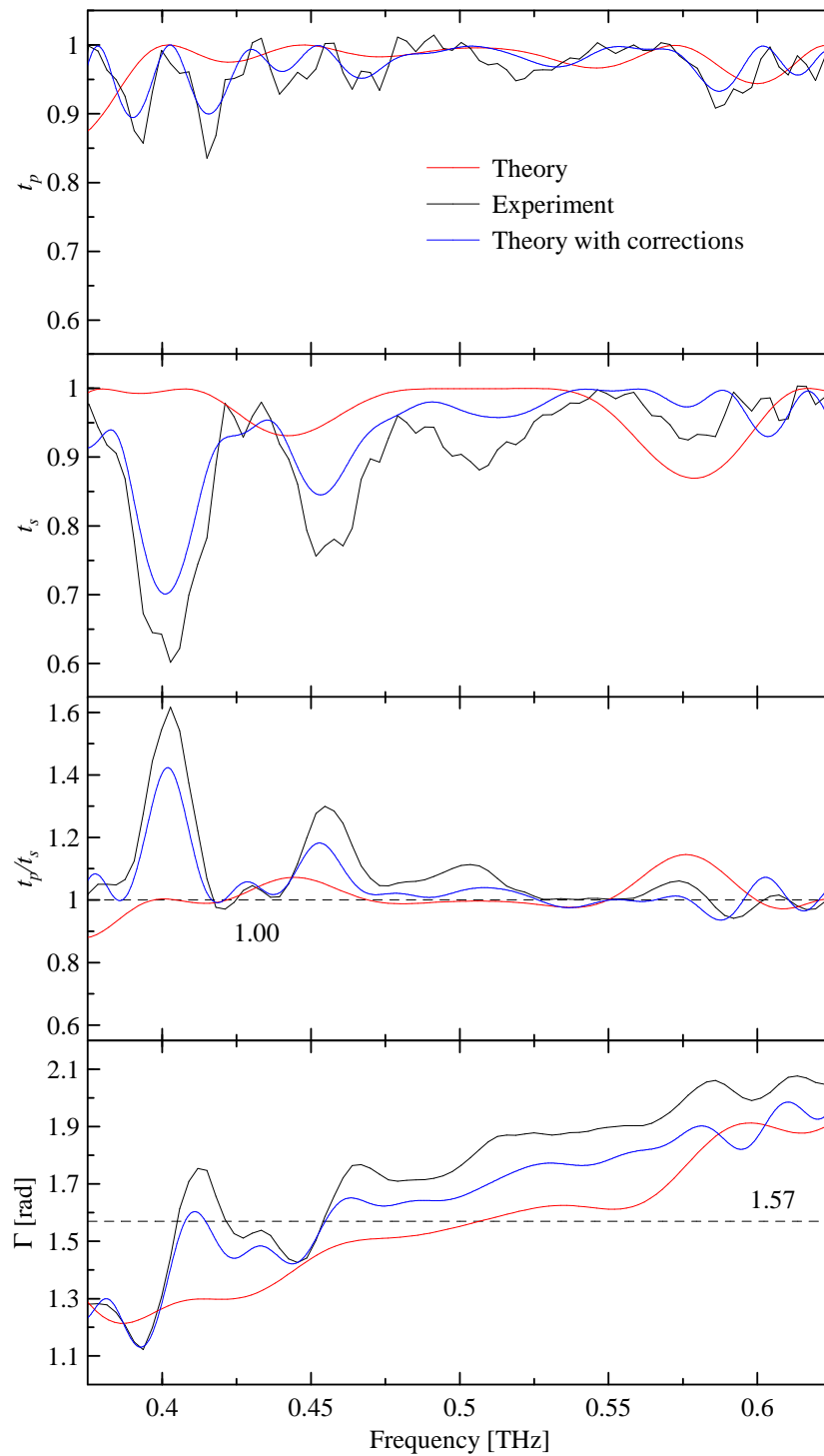


Figure 5.22: Characterization of a selected quarter-wave plate for $f_0 = 0.5$ THz.

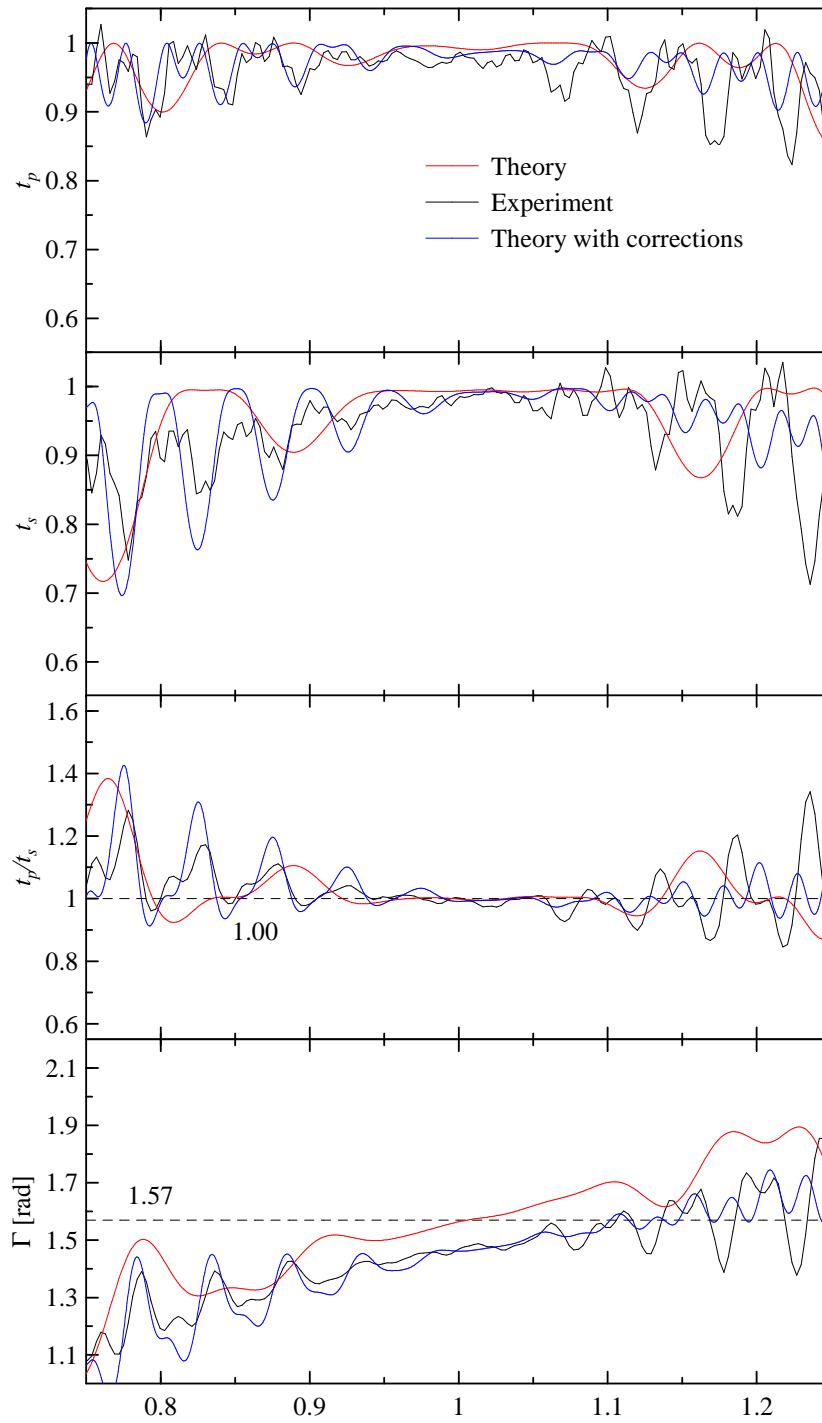


Figure 5.23: Characterization of a selected quarter wave-plate for $f_0 = 1$ THz.

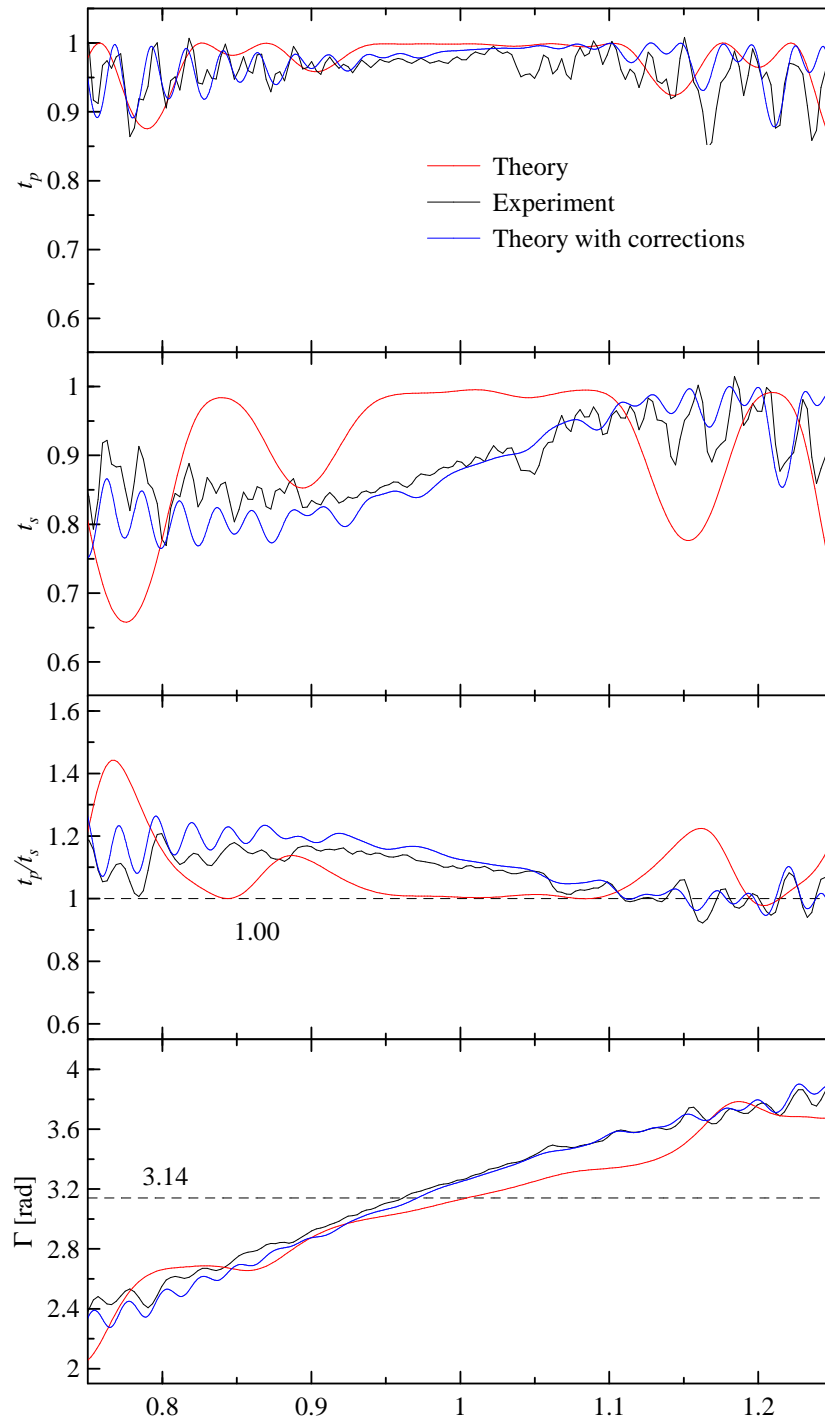


Figure 5.24: Characterization of a selected half-wave plate for $f_0 = 1$ THz.

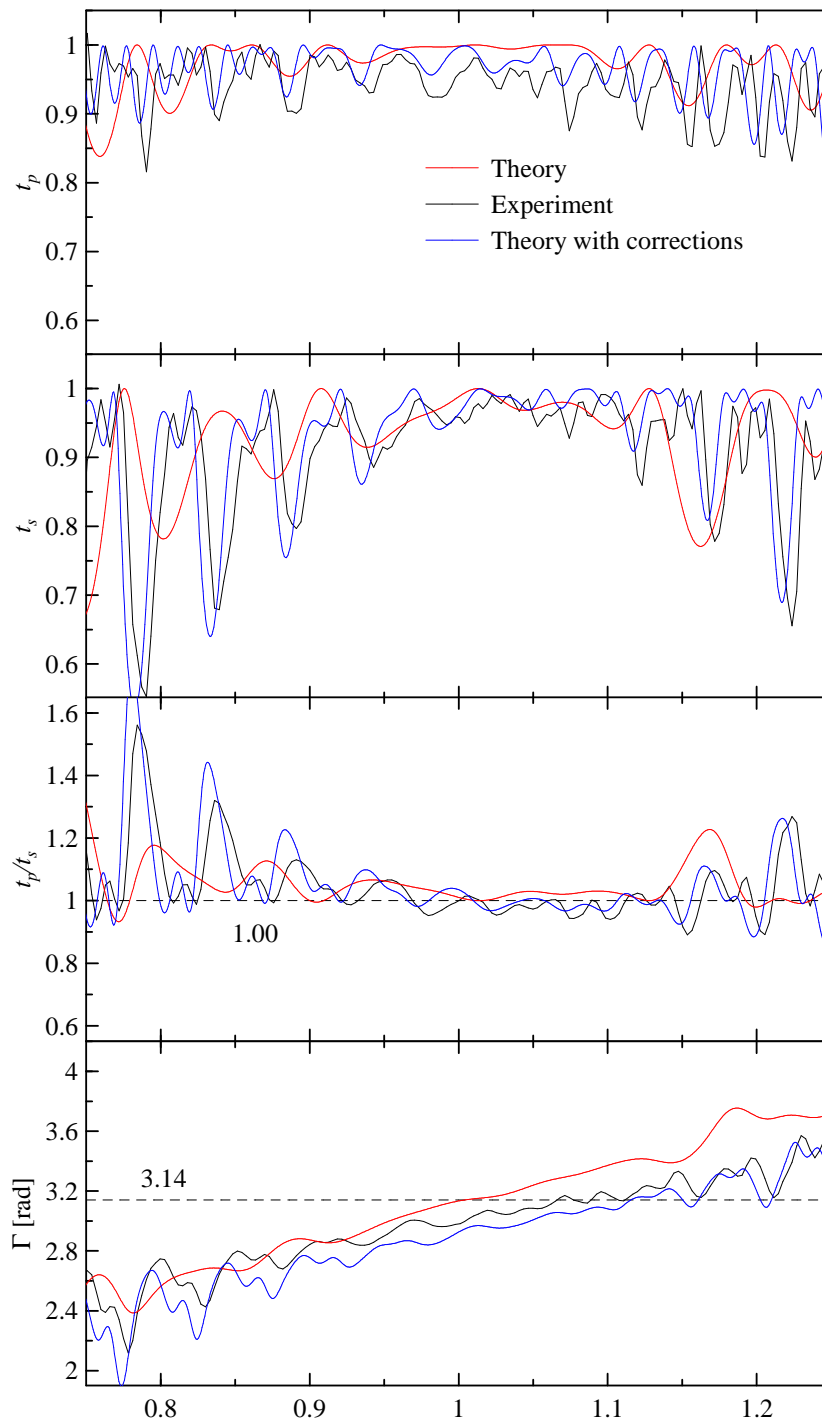


Figure 5.25: Characterization of a double quarter-wave plate for $f_0 = 1$ THz.

5.7 Next research

Our results show that it is possible to prepare a wave plate in the THz range as an etched-Si based composite. The amplitude transmission at the central frequency can be relatively high, above 95 %. On the other hand, the phase retardation is very sensitive to any mismatch in a birefringence of etched layers, especially for the deep ones.

In sec. 4.3.2 we proposed some corrections in the period of etching and filling factors with respect to the theoretical results obtained within the quasi-static approximation. After the experiments we observe that this was not necessary for the B layer and in the next step we would prefer a period of 16 μm instead of 15 μm (with the same air gap width). On the other hand, the compensation for the increase of refractive indices at higher frequencies in layers D (30 μm period instead of 28 μm period) was useful.

Technologically, the most difficult procedure was the etching of D layers, which are deep and where, despite of all efforts, underetching is observed leading to a lower filling factor of the prepared structures. The next iteration in the design of wave plates would be to keep the current protocol for the preparation of D layers and slightly modify the properties of the B layers (which benefit of much better control during fabrication) to obtain the correct phase shift and t_p/t_s ratio at the target frequencies.

In fact, in the current work we designed B layers to be identical for all prepared wave plates. Probably, this would be no longer possible for re-optimized structures with new B layers.

Chapter 6

Conclusion

In this work we combined THz time domain spectroscopy technique together with metamaterials to prepare structures with demanded electric response. We continued the recent work of Ch. Kadlec et al. [49] and we presented a detailed design of a wave plate using birefringent etched layers on Si substrates.

We used the transfer matrix formalism for theoretical optimization of parameters of individual layers in a wave plate and it can be easily used again for optimization of any other wave plate of the same design.

We have experimentally characterized the samples with etched layers and determined their refractive indices and losses (which are negligible) in THz range. Some values of the measured indices differ from theoretically proposed values (<10 %) because of manufacturing errors (mainly underetching).

We have experimentally realized quarter-wave plates for frequencies 0.5 THz and 1 THz and a half-wave plate for 1 THz. The manufacturing errors in samples (especially in D layers) shifted the correct phase retardation to a slightly modified frequencies than considered. The functionality of a quarter-wave plate for 0.5 THz was shifted to 0.43 THz. In similar manner the central frequency of half-wave plate was 0.96 THz instead of 1 THz and the quarter-wave plate for 1 THz have shifted retardation to approximately 1.06 THz. The quarter-wave plate for 1 THz worked as expected at a slightly shifted frequency but still with amplitude transmission higher than 90%. We showed that by using two pairs of birefringent layers (B and D) from a quarter-wave plate for 1 THz it is possible to prepare a half-wave plate working at approximately the same frequency. The manufacturing errors also significantly narrowed the THz spectral width of high transmission around the central frequency.

We also demonstrated that by etching an isotropic structures the antireflective layers can be created.

Bibliography

- [1] L. Fekete: *Ultrafast carrier dynamics in semiconductors studied by Time-resolved terahertz spectroscopy*, Ph.D. thesis, Charles University in Prague, Faculty of Mathematics and Physics (2008).
- [2] D. H. Auston, K. P. Cheung, and P. R. Smith: *Picosecond photoconducting Hertzian dipoles*, Appl. Phys. Lett. 45, 284 (1984).
- [3] A. Dreyhaupt, S. Winnerl, T. Dekorsy, and M. Helm: *High-intensity terahertz radiation from a microstructured large-area photoconductor*, Appl. Phys. Lett. 86, 121114 (2005).
- [4] M. Bass, P. A. Franken, J. F. Ward, and G. Weinreich: *Optical rectification*, Phys. Rev. Lett. 9, 446 (1962).
- [5] M. A. Belkin, J. A. Fan, S. Hormoz, F. Capasso, S. P. Khanna, M. Lachab, A. G. Davies, and E. H. Linfield: *Terahertz quantum cascade lasers with copper metal-metal waveguides operating up to 178 K*, Optics Express 16, 3242 (2008).
- [6] F. E. Doany, D. Grischkowsky, C. C. Chi: *Carrier lifetime versus ion-implantation dose in silicon on sapphire*, Appl. Phys. Lett. 50, 460 (1987).
- [7] H. Němec, F. Kadlec, C. Kadlec, P. Kužel, P. Jungwirth: *Ultrafast far-infrared dynamics probed by terahertz pulses: A frequency domain approach. II. Applications*, J. Chem. Phys. 122, 10 4504 (2005).
- [8] F. C. A. Pockels: *Abhand. d. Ges. d. Wiss. zu Göttingen*, Math. Phys. Klasse 39, 1 (1893).
- [9] H. Němec: *Time-resolved terahertz spectroscopy applied to the investigation of magnetic materials and photonic structures*, Ph.D. thesis, Charles University in Prague, Faculty of Mathematics and Physics (2006).
- [10] Z. Jiang, F. G. Sun, Q. Chen, and X.-C. Zhang: *Electro-optic sampling near zero optical transmission point*, Appl. Phys. Lett. 74, 1191 (1999).

-
- [11] Z. Jiang and X.-C. Zhang: *Electro-optic measurement of THz field pulses with a chirped optical beam*, Appl. Phys. Lett. 72, 1945 (1998).
- [12] Z. G. Lu, P. Campbell, and X.-C. Zhang: *Free-space electro-optic sampling with a high-repetition-rate regenerative amplified laser*, Appl. Phys. Lett. 71, 593 (1997).
- [13] P. Y. Han, , M. Tani, F. Pan, and X.-C. Zhang: *Use of the organic crystal DAST for terahertz beam applications*, Opt. Lett. 25, 675 (2000).
- [14] P. U. Jepsen, C. Winnewisser, M. Schall, V. Schyja, S. R. Keiding, and H. Helm: *Detection of THz pulses by phase retardation in lithium tantalate*, Phys. Rev. E 53, 3052 (1996).
- [15] C. Winnewisser, P. U. Jepsen, M. Schall, V. Schyja, and H. Helm: *Electro-optic detection of THz radiation in LiTaO₃, LiNbO₃ and ZnTe*, Appl. Phys. Lett. 70, 3069 (1997).
- [16] S. Nashima, O. Morikawa, K. Takata, and M. Hangyo: *Measurement of optical properties of highly doped silicon by terahertz time domain reflection spectroscopy*, Appl. Phys. Lett. 79, 3923 (2001).
- [17] C. A. Schmuttenmaer: *Exploring dynamics in the far-infrared with terahertz spectroscopy*, Chem. Rev. 104, 1759 (2004).
- [18] R. Appleby and H. B. Wallace: *Standoff Detection of Weapons and Contraband in the 100 GHz to 1 THz Region*, IEEE Trans. Antennas Prop. 55, 2944 (2007).
- [19] A. G. Davies, A. D. Burnett, W. Fan, E. H. Linfield, J. E. Cunningham: *Terahertz spectroscopy of explosives and drugs*, Mater. Today 11, 18 (2008).
- [20] R. M. Woodward, B. E. Cole, V. P. Wallace, R. J. Pye, D. D. Arnone, E. H. Linfield, M. Pepper: *Terahertz pulse imaging in reflection geometry of human skin cancer and skin tissue*, Phys. Med. Biol. 47, 5853 (2002).
- [21] E. Pickwell, V. P. Wallace, B. E. Cole, S. Ali, C. Longbottom, R. Lynch, M. Pepper: *A Comparison of Terahertz Pulsed Imaging with Transmission Microradiography for Depth Measurement of Enamel Demineralisation in vitro*, Caries Res. 41, 49 (2007).
- [22] M. J. Fitch, R. Osiander: *Terahertz waves for communications and sensing*, Johns Hopkins APL Technical Digest 25, 348-355 (2004).

- [23] J. Li, C. T. Chan: *Double-negative acoustic metamaterial*, Phys. Rev. E 70, 055602 (2004).
- [24] H. Chen, C. T. Chan: *Acoustic cloaking in three dimensions using acoustic metamaterials*, Appl. Phys. Lett. 91, 183518 (2007).
- [25] W. Cai, V. Shalaev: *Optical Metamaterials: Fundamentals and Applications*, Springer, New York (2010).
- [26] V. G. Veselago: *Electrodynamics of substances with simultaneously negative values of sigma and mu*, Sov. Phys. Usp. 10:509–514 (1968).
- [27] A. Grbic, G. V. Eleftheriades: *Experimental verification of backward-wave radiation from a negative refractive index metamaterial*, J. Appl. Phys. 92, 5930 (2002).
- [28] L. Ran, J. Huangfu, H. Chen, X. Zhang, and K. Cheng, T. M. Grzegorzczuk, J. A. Kong: *Experimental study on several left-handed metamaterials*, PIER 51, 249 (2005).
- [29] J. B. Pendry: *Negative refraction makes a perfect lens*, Phys. Rev. Lett. 85, 3966 (2000).
- [30] J. B. Pendry, D. R. Smith: *Reversing light with negative refraction*, Phys. Today 57, 37 (2004).
- [31] D. R. Smith, W.J. Padilla, D.C. Vier, S.C. Nemat-Nasser, S. Schultz: *Composite medium with simultaneously negative permeability and permittivity*, Phys Rev Lett 84, 4184 (2000).
- [32] R. A. Shelby, D. R Smith, S. Schultz: *Experimental verification of a negative index of refraction*, Science 292, 77 (2001).
- [33] J.C. Maxwell Garnett: *Colours in metal glasses and in metallic films*, Phil Trans R Soc Lond 203, 385–420 (1904).
- [34] D. A. G. Bruggeman: *Calculation of various physics constants in heterogeneous substances I. Dielectricity constants and conductivity of mixed bodies from isotropic substances*, Annalen Der Physik 24, 636–664 (1935).
- [35] V. M. Shalaev: *Nonlinear optics of random media: fractal composites and metal-dielectric films*, Springer, Berlin (2000).
- [36] J. B. Pendry, A. MacKinnon: *Calculation of photon dispersion relations*, Phys. Rev. Lett. 69, 2772 (1992).

- [37] W. Rotman: *Plasma simulation by artificial dielectrics and parallel-plate media*, IRE Trans. Antennas Propag. 10, 82 (1962).
- [38] J. B. Pendry, A. J. Holden, D. J. Robbins, W. J. Stewart: *Magnetism from conductors and enhanced nonlinear phenomena*, IEEE Trans. Microw. Theory Tech. 47, 2075 (1999).
- [39] S. Zhang, W. J. Fan, K. J. Malloy, S. R. J. Brueck, N. C. Panoiu, R. O. Osgood: *Demonstration of metal-dielectric negative-index metamaterials with improved performance at optical frequencies*, J. Opt. Soc. Am. B 23, 434 (2006).
- [40] S. Zhang, W. Fan, B. K. Minhas, A. Frauenglass, K. J. Malloy, and S. R. J. Brueck: *Midinfrared resonant magnetic nanostructures exhibiting a negative permeability*, Phys. Rev. Lett. 94, 037402 (2005).
- [41] S. Linden, Ch. Enkrich, M. Wegener, J. Zhou, T. Koschny, C. M. Soukoulis: *Magnetic response of metamaterials at 100 terahertz*, Science 306, 1351 (2004).
- [42] S. Durant, Z. W. Liu, J. A. Steele, X. Zhang: *Theory of the transmission properties of an optical far-field superlens for imaging beyond the diffraction limit*, J. Opt. Soc. Am. B 23, 2383 (2006).
- [43] Z. W. Liu, S. Durant, H. Lee, Y. Pikus, N. Fang, Y. Xiong, C. Sun, X. Zhang: *Far-field optical superlens*, Nano Lett 7, 403 (2007).
- [44] V. M. Shalaev: *Transforming light*, Science 322, 384 (2008).
- [45] D. Schurig, J. J. Mock, B. J. Justice, S. A. Cummer, J. B. Pendry, A. F. Starr, D. R. Smith: *Metamaterial electromagnetic cloak at microwave frequencies*, Science 314, 977 (2006).
- [46] H. T. Chen, W. J. Padilla, J. M. O. Zide, A. C. Gossard, A. J. Taylor, R. D. Averitt: *Active terahertz metamaterial devices*, Nature 444, 597 (2006).
- [47] H. T. Chen, W. J. Padilla, J. M. O. Zide, S. R. Bank, A. C. Gossard, A. J. Taylor, R. D. Averitt: *Ultrafast optical switching of terahertz metamaterials fabricated on ErAs/GaAs nanoisland superlattices*, Opt. Lett. 32, 1620 (2007).
- [48] H. Němec, P. Kužel, F. Kadlec, C. Kadlec, R. Yahiaoui, P. Mounaix: *Tunable terahertz metamaterials with negative permeability*, Phys. Rev. B 79, 241108(R) (2009).

-
- [49] Ch. Kadlec, F. Kadlec, P. Kužel, K. Blary and P. Mounaix: *Materials with on-demand refractive indices in the terahertz range*, Opt. Lett. 33, 2275 (2008).
- [50] B. E. A. Saleh, M. C. Teich: *Fundamentals of Photonics*, John Wiley & Sons, Inc., New York, 1991.
- [51] M. Born, E. Wolf: *Principles of Optics*, 7th ed., University Press, Cambridge, 2003.
- [52] L. Fekete, F. Kadlec, H. Němec, P. Kužel: *Fast one-dimensional photonic crystal modulators for the terahertz range*, Opt. Express 15, 8898 (2007).